



PROMICE | GC-NET automatic weather station data

Robert S. Fausto¹, Penelope How¹, Baptiste Vandecrux¹, Mads C. Lund¹, Jason E. Box¹, Kenneth D. Mankoff^{1,8,9}, Signe B. Andersen¹, Dirk van As¹, Rasmus Bahbah¹, Michele Citterio¹, William Colgan¹, Henrik T. Jakobsgaard¹, Nanna B. Karlsson¹, Kristian K. Kjeldsen¹, Signe H. Larsen¹, Charlotte Olsen¹, Falk Oraschewski¹, Anja Rutishauser¹, Christopher L. Shields¹, Anne M. Solgaard¹, Ian T. Stevens¹, Synne H. Svendsen¹, Kirsty Langley², Alexandra Messerli², Anders A. Bjørk³, Jonas K. Andersen³, Jakob Abermann⁴, Jakob Steiner⁴, Rainer Prinz⁵, Berhard Hynek^{6,4,10}, James M. Lea⁷, Stephen Brough⁷, and Andreas P. Ahlstrøm¹

Correspondence: Robert S. Fausto (rsf@geus.dk)

Abstract. We present a new version of the PROMICE | GC-NET automatic weather station (AWS) data product, combining observations from two Greenland AWS networks; PROMICE and GC-NET. The dataset integrates records from more than 50 active and historical AWS sites across the Greenland Ice Sheet, peripheral glaciers and land areas. This new version includes improvements in station design, sensor configuration, and data processing. Two primary station types are used: dual-boom masts in the accumulation area, and free-standing tripods with a single instrument boom in the ablation area. Data are processed with pypromice, an open-source Python package designed for standardized, transparent, and reproducible workflows, including calibration, filtering, variable derivation, and correction. The resulting products are distributed in CF-compliant NetCDF and CSV formats and include both measured and derived variables for applications in polar meteorology, climatology, and glaciology. Access is open under license CC-BY 4.0. A GitHub-based issue tracker (https://github.com/GEUS-Glaciology-and-Climate/PROMICE-AWS-data-issues) supports community-driven quality control within a living data framework. The datasets are openly available at https://doi.org/10.22008/FK2/IW73UU (How et al., 2022a).

¹The Geological Survey of Denmark and Greenland, Øster Voldgade 10, 1350 Copenhagen, Denmark

²Hydrology, Climate and Environment, Asiaq Greenland Survey, Nuuk, Greenland

³Department of Geosciences and Natural Resource Management (IGN), University of Copenhagen, Copenhagen, Denmark

⁴Department of Geography and Regional Science, University of Graz, Graz, Austria

⁵Department of Atmospheric and Cryospheric Sciences, University of Innsbruck, Innsbruck, Austria

⁶Geosphere Austria, Department Climate Impact Research, Vienna, Austria

⁷Department of Geography and Planning, School of Environmental Sciences, University of Liverpool, Liverpool, UK

⁸NASA Goddard Institute for Space Studies, New York, NY, 10025 USA

⁹Autonomic Integra LLC, New York, NY, 10025 USA

¹⁰Austrian Polar Research Institute, Vienna, Austria

© Author(s) 2025. CC BY 4.0 License.





1 Introduction: what is new and background

What is new

Compared to Fausto et al. (2021), we present the latest version of the PROMICE | GC-NET AWS data product. In 2021, the Geological Survey of Denmark and Greenland (GEUS) integrated the Greenland Climate Network (GC-NET) into its monitoring program (Steffen et al., 1996; Steffen and Box, 2001; Vandecrux et al., 2023), with contributions from Greenland Ecosystem Monitoring (GEM) (Abermann et al., 2019; Fausto et al., 2020; Messerli et al., 2022; Larsen et al., 2024), prompting the development of a standardized and transparent Greenland-wide AWS data product. The unified PROMICE | GC-NET dataset now consists of over 50 stations across accumulation and ablation areas, local peripheral glaciers, and ice-free areas in Greenland (Fig. 1); including both GEUS and externally owned stations (See 1 for more information).

Station designs vary by location: accumulation area stations use single masts with two instrument booms, while other stations are tripod-based with a single intrument boom for bare-ice and ice-free conditions. Sensor and system upgrades include new fan-aspirated temperature and humidity sensors, pluviometers, tilt-correcting radiometers, CR1000X data loggers, and digital 10 m thermistor strings. Ablation zone stations are equipped with new high-density Nickel-metal hydrate (NiMH) batteries, and all new stations transmit data hourly via the Iridium Short Burst Data system.

Data processing is handled via the open-source Python package pypromice (How et al., 2023b; Python Software Foundation, 2024), which supports calibration, automated/manual quality control, and merging of data across station upgrades to ensure long-term consistency. The publicly available dataset is available in CF-compliant NetCDF and CSV formats (How et al., 2022a, 2023a; Unidata, 2023; Eaton et al., 2024). Near-real-time AWS data are available via the GEUS Thredds server (https://thredds.geus.dk), which provides OPeNDAP access to operational datasets (Cornillon et al., 2003; Nativi et al., 2006; OPeNDAP, Inc., 2024). The dataset is updated hourly with the latest transmission data from the AWS network. Measurements are collected, processed, and published with a typical latency of 10 –15 minutes.

The dataset has been prepared to follow the FAIR principles: Findable, Accessible, Interoperable, Reusable (Wilkinson et al., 2016). To support transparency and community engagement, data issues are tracked via a GitHub-based system. Users can report and review issues, which are tagged by station, sensor, and year. Verified issues are addressed in future releases and remain publicly accessible at https://github.com/GEUS-Glaciology-and-Climate/PROMICE-AWS-data-issues. We recommend all users to look at the README file associated with the dataset for the newest updates and contents (How et al., 2022b).

Background

35

The Greenland Ice Sheet has contributed $0.42 \pm 0.04 \,\mathrm{mm}\,\mathrm{yr}^{-1}$ to rising sea levels since 1992 (Shepherd et al., 2020), due to changes in surface mass balance (SMB) (Fettweis et al., 2017) and solid ice discharge (Mouginot et al., 2019; Mankoff et al., 2020). Depending on the climate scenario, the ice sheet is expected to contribute another 78 to $175 \,\mathrm{mm}$ to sea level rise in





60

Science Science Data

Data

the future (Box et al., 2022). Greenland-scale SMB variations are evaluated using regional climate models, but these models exhibit considerable uncertainties, leading to differences across projections (e.g., Fettweis et al., 2020; Shepherd et al., 2020; Vandecrux et al., 2020). The uncertainties are particularly pronounced in areas with high mass loss close to the ice sheet margin (Fettweis et al., 2020). Consequently, *in-situ* measurements of accumulation, ablation, and energy balance on the ice sheet are essential for improving our understanding of surface processes (Hanna et al., 2020). On-ice AWSs are crucial for gathering such data (e.g., Smeets and Van den Broeke, 2008a; Fausto et al., 2016a).

GEUS has been monitoring Greenland's glaciers, ice caps, and ice sheet since the late 1970s (Citterio et al., 2015). Early efforts, such as ablation stake transects and automated weather measurements (e.g., Braithwaite and Olesen, 1989), faced challenges with accessibility and technological limitations, leading to intermittent and sparse data. By the 1990s, advances in automatic weather station (AWS) technology enabled year-round monitoring. Other AWS initiatives followed, including the Greenland Climate Network (GC-Net), that began at Swiss Camp in 1990 and expanded to additional sites by 1995 (Steffen et al., 1996), installations along the K-transect in 1993 (Smeets et al., 2018), Summit in 2008, and the SIGMA project in northwest Greenland in 2012 (Aoki et al., 2014). More recently, starting in 2021, Chinese researchers installed AWSs on the Greenland Ice Sheet near Kangerlussuaq (Chen et al., 2023).

Prior to 2007, most AWSs were situated in the accumulation area of the Greenland Ice Sheet, where snowfall dominates mass balance. Few stations existed in the ablation area, where melting is the primary factor in mass loss, underscoring the need for long-term monitoring in these regions. To address the lack of data in low-elevation ablation areas, Programme for monitoring of the Greenland ice sheet (PROMICE) installed AWSs to complement existing networks and provide critical measurements across diverse climate zones (Ahlstrøm et al., 2008). Launched in 2007, PROMICE established a network of 14 AWSs placed strategically in seven regions: stations at Kronprins Christian Land (KPC), Scoresbysund (SCO), Tasiilaq (TAS), Qassimiut (QAS), Nuuk (NUK), Upernavik (UPE), and Thule (THU) are complemented by additional AWSs from three Austrian research groups (FRE; Hynek et al., 2024), (WEG B and WEG L; Abermann et al., 2023) and (RED L; Prinz et al., 2023) projects, as well as other installations near Kangerlussuaq (KAN_B, KAN_L, KAN_M, and KAN_U) as part of the Greenland analogue project (Claesson Liljedahl et al., 2016), which were included in PROMICE in 2021. Each region includes lower (L) stations near the ice margin and upper (U) stations closer to the equilibrium line altitude (ELA). Additional collaborative projects have expanded the number of AWSs where some are located at middle (M), accumulation (A), or bedrock (B) sites, including seven located on peripheral glaciers (NUK_K, MIT, ZAC_L, ZAC_U, ZAC_A, LYN_L, LYN_T) through GEM (Abermann et al., 2019; Fausto et al., 2020; Messerli et al., 2022; Larsen et al., 2024). Asiaq Greenland Survey maintains the NUK_K station (Table 1), which has been continuously operated since 2012 through a long-standing collaboration with GEUS under the GEM programme.

In 2021, GEUS assumed responsibility for GC-NET, integrating its sites with PROMICE operations. This transition ensured the continuation of GC-NET's legacy of high-quality data collection while leveraging our expertise and resources to maintain

https://doi.org/10.5194/essd-2025-687

Preprint. Discussion started: 28 November 2025

© Author(s) 2025. CC BY 4.0 License.



Science Science Data

80 monitoring capabilities.In addition, a recent collaboration between the GEUS and the University of Copenhagen Department

of Geosciences and Natural Resource Management (IGN) has led to the installation of two additional AWSs on bedrock near

the peripheral glacier Mittivakkat in Southeast Greenland (SER_B and MIT_B). Lastly, the NUK_B AWS located on bedrock

in the Nuuk fjord is a collaboration between GEUS, Asiaq Greenland Survey, and the University of Liverpool (Table 1).

85 The AWSs operate year-round, measuring surface mass balance, near-surface climatology, and glacier flow. Built to endure

harsh Arctic conditions, they are transportable by plane, helicopter, snowmobile, car, or dogsled. With over 50 stations, the

network enhances the ability to monitor Greenland's surface climate variability (e.g., Van As et al., 2011, 2013, 2014b), con-

tributing to assessments (e.g., Poinar et al., 2024, 2025) and supporting validation of satellite data, climate models, and ice

sheet mass balance inter-comparison exercises (e.g., Van As et al., 2014a; Ryan et al., 2017; Noël et al., 2018; Solgaard et al.,

2021; Otosaka et al., 2023).

90

This new version of the PROMICE | GC-NET AWS dataset from maintained AWSs that monitor the atmosphere and ice

masses in Greenland provides continuous data essential for understanding the Arctic environment. The freely available dataset

can be accessed at https://thredds.geus.dk, last access: 29 August 2025, which is updated every hour or for a citable and man-

ually QC'ed version updated monthly: https://doi.org/10.22008/FK2/IW73UU. This dataset description provides a detailed overview of the PROMICE | GC-NET AWS dataset, including insights into measurements, post-processing, sensor calibration,

and begins with a technical description of the AWS instruments, followed by details on the data production chain (pypromice),

examples of station measurements, and concludes with a summary and outlook.

2 AWS design

100 The PROMICE | GC-NET AWS systems measures (1) the meteorological parameters required for calculating the surface energy

budget, (2) snow ablation/accumulation and ice ablation, (3) subsurface temperature to a depth of 10 m, and (4) position by

single frequency GPS. The following subsections provide detailed information on the instruments and hardware used, the

AWS assembly process, the measurement frequency and accuracy of each sensor. We then present the design of the two AWS

systems, including the placement of instruments, hardware, and other key considerations. Finally, we provide information on

the transmission schedule and maintenance plan.

2.1 Instruments & Hardware

Here, we describe all relevant sensors and other components used in our AWS setups (Table 2). Further sensor details are

provided in the Appendix. Some sensors are AWS system specific; the ablation area stations consist of free-standing tripods

with one sensor boom, while the accumulation area stations have two sensor booms attached at different levels on a mast drilled

into the firm (AWS design details described in sections 2.2.1 and 2.2.2).





2.1.1 Barometer (air pressure)

Barometric pressure (in hPa) is measured in the fibreglass reinforced polyester logger enclosure using a CS100/Setra 278 barometer. The logger enclosure adjusts to ambient pressure through a pressure-compensating plug. The barometer manufacturer reports a measurement accuracy of ± 2 hPa within the -40 °C to +60 °C temperature range (Table 2). The barometer in the OTT Lufft WS401 is a high-precision digital sensor designed for measurement of atmospheric pressure. It operates based on MEMS (micro-electromechanical systems) technology and provides reliable data over a pressure range of 300–1100 hPa. The accuracy is ± 0.5 hPa within the temperature range of 0 to 40 °C, and ± 1.5 hPa outside that range.

2.1.2 Thermometer (air temperature)

Air temperature in $^{\circ}$ C is measured inside a fan-aspirated radiation shield using the Rotronics setup (Fausto et al., 2021). The primary temperature sensor is a PT100 probe, which has an accuracy of ± 0.1 $^{\circ}$ C (Table 2). A secondary air temperature reading is obtained from the HygroClip temperature/humidity sensor, also housed in the aspirated shield. This sensor also has a manufacturer-stated accuracy of ± 0.1 $^{\circ}$ C but needs more frequent recalibration than the PT100 (Fausto et al., 2021).

The thermometer in the OTT Lufft WS401 is a capacitive sensor designed for air temperature measurement. It has a measurement range of -50 °C to +60 °C, with an accuracy of ± 0.2 °C at 20 °C. The sensor is enclosed in an aspirated shield.

The Vaisala HMP 155E HUMICAP sensor measures air temperature (in °C) using a Platinum Resistance Thermometer (PT100) inside a fan-aspirated radiation shield from Rika. The measurement range is -80 °C to +60 °C, with accuracy varying with temperature. Specifically, for the range of -80 °C to +20 °C, the accuracy is $\pm (0.226 - 0.0028 \times \text{air temperature})$ °C.

130 2.1.3 Hygrometer (humidity)

In the Rotronics setup (Fausto et al., 2021), relative humidity (RH; in %) is measured alongside the PT100 sensor inside the aspirated radiation shield using a HC2A-S3 (or HC2) HygroClip, which has an accuracy of $\pm 0.8\%$.

The OTT Lufft WS401 hygrometer features a capacitive humidity sensor designed for humidity measurement, operating over a range of 0–100% relative humidity with an accuracy of $\pm 2\%$ in the 10–90% range at 20 °C. It is temperature-compensated and housed in an aspirated enclosure.

The Vaisala HMP155E uses a HUMICAP sensor for relative humidity measurement, offering an accuracy of up to $\pm 1\%$. It operates over the 0–100% range. With an operating temperature range of -80 °C to +60 °C, the sensor provides fast response times, temperature compensation, and resistance to contamination.

Relative humidity is measured with respect to water, meaning calibration is performed above the freezing point. Hygrome-

© Author(s) 2025. CC BY 4.0 License.



Science Science Data

ters are typically recalibrated when possible, but in practice this occurs every 1 to 4 years. Calibration is conducted in a closed chamber at room temperature under controlled relative humidity conditions at levels of 10%, 35%, and 80%. Alternatively, the instruments may be sent to the manufacturer for recalibration.

For temperatures below freezing, relative humidity is recalculated relative to ice in post-processing. To distinguish between the two relative humidities in the data products, the prior humidity (adjusted below freezing) is called "relative humidity with respect to water or ice", whereas the latter is simply referred to as "relative humidity". The conversion of relative humidity relative to ice is after Goff and Gratch (1946). See Table 2 for further information.

2.1.4 Pluviometer (liquid precipitation)

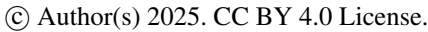
The OTT Lufft WS401 is a tipping bucket rain gauge (in mm) designed for real-time liquid precipitation measurement. Rainfall collects in a small, seesaw-like bucket that tips once a set volume (typically 0.1 or 0.2 mm) is reached, triggering a magnetic switch to record one 'tip.' The total rainfall is calculated by counting these tips over time. This design performs well in most weather conditions, though regular maintenance is needed to prevent clogging or debris buildup. It is not optimal for measuring solid precipitation (e.g., snowfall) since the instrument lacks heating, which can lead to snow accumulation and delayed melting within the gauge. Nevertheless, it is adopted here as a rain gauge in a large range of conditions experienced across Greenland (Table 2).

2.1.5 Anemometer (wind speed and direction)

We use anemometers from the manufacturer Young. The wind speed and direction (in m s⁻¹ and degrees, respectively) measurement height, like the other measurements, has a reduced measurement height if a winter snow layer is present (Table 2). An AC sine wave voltage signal is produced by the rotation of the four-bladed propeller, and the pulse count converts to wind speed using a multiplier. According to the manufacturer, the sensor can measure wind speeds between 0 and 100 m s⁻¹, with an accuracy of ± 0.3 m s⁻¹ or 1% if the measured value is higher than 30 m s⁻¹. Wind direction is measured through changes in the vane angle by a potentiometer housed in a sealed chamber on the instrument. The output voltage is directly proportional to vane angle wind direction and is measured between 0 and 360° with an accuracy of $\pm 3^{\circ}$. When possible, every three years the sensor is replaced and tested for drift and functionality with an "anemometer drive", rotating the propeller shaft at a known rate. The instrument's orientation is logged and reset to "geographic north" during each maintenance visit to keep wind direction data accurate within $\pm 15^{\circ}$ (although much larger station rotations have been encountered).

2.1.6 Radiometer (visual- and infrared light)

The Kipp & Zonen CNR1 and CNR4 are net radiometers (in Wm^{-2}), designed to measure the balance between shortwave and longwave radiation. The CNR1 is an instrument with two pyranometers and two pyrgeometers, suitable for meteorological and environmental research. The CNR4 is an advanced model offering improved accuracy, including lower thermal offset, and





180



better longwave response. These radiometers are targeted for recalibration every three years (Table 2), however in a few cases, recalibration happens every 4-5 years.

The pyranometers, housed within hemispherical glass domes to minimize water droplet adhesion, record upward and downward shortwave irradiance between 0.3 and 2.5 μ m. The manufacturer specifies a sensor uncertainty of 10%, though practical assessments in Antarctica suggest an approximate 5% uncertainty for daily totals (van den Broeke et al., 2004).

The pyrgeometers measure upward and downward longwave irradiation with an estimated field uncertainty of 10% for the CNR1 and 5% for the CNR4. These values account for instrumental and environmental factors, including calibration accuracy and thermal offsets. Both pyrgeometers use silicon windows, sensitive to infrared wavelengths between 4.5 and 42 μ m.

The radiometer data is stored in the data logger as voltage (μV) due to the unique calibration coefficients assigned to each radiometer, while all logger programs on the AWSs remain standardized for operational efficiency. During post-processing, raw sensor readings (SR_{raw}) are converted into physical measurements (SR_m) using the equation:

$$SR_m = \frac{SR_{raw}}{C_{SR}},\tag{1}$$

where C_{SR} (unit: $\mu V(Wm^{-2})^{-1}$) is the sensor specific calibration coefficion provided by the manufactorer. SR_m represents either the downward or upward shortwave irradiance. Similar to shortwave radiation, longwave radiation readings are stored in the data logger as voltage (LR_{raw}) and later converted into physical units (LR_m) during post-processing using the formula:

$$LR_m = \frac{LR_{raw}}{C_{LR}} + 5.67 \cdot 10^{-8} \cdot (T_{rad} + T_0)^4,$$
(2)

where C_{LR} (unit: $\mu V(Wm^{-2})^{-1}$) is the sensor calibration coefficient. T_{rad} represents the sensor temperature recorded within the radiometer casing (°C), and $T_0 = 273.15$ K.

195 2.1.7 Sonic ranger (surface height)

The Campbell Scientific SR50A is an ultrasonic depth sensor (sonic ranger) designed for measurement of height changes, e.g. snow accumulation (Table 2). It operates by emitting ultrasonic pulses toward the surface and measuring the time delay of the reflected signal. The SR50A is durable, weather-resistant, and suitable for use in harsh environmental conditions, making it ideal for AWSs on the Greenland ice sheet. On both station designs, the sensor boom height (in meters) is measured by a sonic ranger mounted approximately 0.1 m below the boom itself. For the tripod design, a SR50A is also mounted on a stake assembly drilled into the ice recording surface height changes.

Boom or stake height (H_m in m.) is derived from raw sensor data (H_{raw}), corrected for air temperature during post-processing:

$$H_m = H_{raw} \cdot \sqrt{\frac{T_{air} + T_0}{T_0}},\tag{3}$$

© Author(s) 2025. CC BY 4.0 License.



215

220

235



where $T_0 = 273.15$ K. After temperature correction, the manufacturer-reported uncertainty for the SR50A sonic ranger (Campbell Scientific) is ± 1 cm or $\pm 0.4\%$ of the measured distance. An uncertainty assessment for sonic ranger readings, based on wintertime accumulation-free data from SCO_U, found standard deviations of 1.7 cm and 0.6 cm after spike removal, corresponding to uncertainties of 0.7% and 0.6% of the measured distance, respectively (Fausto et al., 2012).

210 2.1.8 Pressure transducer assembly (surface height)

The Ørum & Jensen NT 1700 is a robust pressure transducer designed for accurate measurement of water pressure and level in environmental and industrial applications (Table 2). It features a piezoresistive sensor element, housed in a durable stainless steel casing, and is suitable for long-term deployment. The NT 1700 offers reliable performance, stable output, and compatibility with standard data logging systems. The tripod AWSs are equipped with a pressure transducer assembly (PTA) that measures surface height changes caused by ice ablation. Originally developed in Greenland in 2001 by Bøggild et al. (2004) and later refined under PROMICE (Fausto et al., 2012), the PTA consists of a hose filled with a 50/50 antifreeze-water mixture and a pressure transducer at its base. The hose is typically drilled up to 14 m into the ice, and the transducer registers the pressure from the vertical liquid column above it. A schematic showing how to construct the PTA system is provided in the appendix. Similar to the radiometer, each PTA has a unique calibration coefficient, which is why measurements (H_{raw}) are stored as voltage in the data logger and is converted into physical units as (H_m in m.):

$$H_m = C_{PTA} \cdot \frac{\rho_w}{\rho_{af}} \cdot H_{raw},\tag{4}$$

where C_{PTA} is the calibration coefficient. The constants ρ_w and ρ_{af} are the densities of water and the antifreeze/water solution, respectively.

2.1.9 Thermistor string (subsurface temperature)

We have two types of thermistor strings (temperature-dependent resistor) that measure subsurface temperatures (in °C). We have a digital and an analogue type: the analogue type is designed and constructed internally, while the digital type is made by Geoprecision (Table 2, Appendix for further details).

For sites in the ablation area, the subsurface ice temperature is measured using a 10-meter thermistor string with 8 thermistors unevenly spaced. The string records temperatures at depths that may vary due to surface ablation and accumulation as seasons change through the year.

For sites in the accumulation area, the subsurface firn temperature is similarly measured using a 10-meter thermistor string (digital type), but with 11 thermistors unevenly spaced to capture the higher temperature variability in the near-surface snow/firn. When installed, the top thermistor is placed at surface level, with a spacing of 50 cm to the next down to 3 m depth, then a spacing of 1 m to 4 m depth, followed by 2 m spacings down to the bottom thermistor at 10 m depth. The thermistor string is inserted into a standard 32 mm (outer diameter) polypropylene pipe (PP), commonly used for sewer water and consisting

https://doi.org/10.5194/essd-2025-687

Preprint. Discussion started: 28 November 2025

© Author(s) 2025. CC BY 4.0 License.



240

250

Science Science Data

of 6 x 2 m pieces, allowing for a 2 m extension above the snow surface. The PP pipe system is sealed at the bottom and a custom-made cap allowing passage of the cable is placed at the top end, providing a waterproof system with the thermistor string extended in a relatively narrow air-filled pipe. The PP pipe is usually reinforced with a stake for structural support and a thin bamboo pole is attached as an extension at the top to help locating the system if the snowfall exceeds the height of the PP pipe before next visit.

2.1.10 Compass/Inclinometer

We use two types of inclinometers. HL Planartechnik GmbH offers a range of high-precision inclinometers, commonly known as tiltmeters, designed to measure angular displacement with accuracy and reliability. For instance, the NS-25/E2 inclinometer features a flexible circuit adaptable to different systems. It provides a voltage output signal. The Planar inclinometer measures the tilt (in degrees) both across (left-right) and along (up-down) the sensor boom, which is interpreted as tilt-to-east and tilt-to-north when the sensor boom is oriented north-south. The inclinometer's voltage readings ($Tilt_{raw}$) are converted into $Tilt_m$ in degrees using the following equation:

$$Tilt_{m} = 21.1 \cdot |Tilt_{raw}| - 10.4 \cdot |Tilt_{raw}|^{2} + 3.6 \cdot |Tilt_{raw}|^{3} - 0.49 \cdot |Tilt_{raw}|^{4}, \tag{5}$$

where all constants were determined in-house (Table 2).

The Rion compass was chosen to replace the HL Planar tiltmeter in our AWS systems. It uses magnetic field sensors to determine azimuthal orientation, providing accurate and reliable heading (tilt) data for applications that require precise directional alignment, such as measuring downward shortwave irradiance and wind direction (see Table 2).

2.1.11 GPS (AWS position)

Since their inception, all AWSs have been equipped with a single frequency GPS that records site position and position metrics hourly. The same technology has been applied to GC-Net stations starting in 2020 for the SWC site and in 2021 onward for an increasing number of the GEUS carry-forward GC-Net sites. The GPS antenna and the receiver, which is part of the Iridium 9602-LP modem, are housed inside the data logger enclosure. The receiver is a NEO-6Q model, operating at 1575.42 MHz (L1), with 16 channels and C/A code. Its accuracy is reported to be within 2.5 meters (Table 2). Implicit in the single frequency measurements is the use of the EGM96 geoid to obtain orthometric height a.k.a. elevation above mean sea level. See also AWS position in the post-processing section for more information.

In the AWS configuration, the GPS receiver is activated for one minute before each Iridium transmission attempting to acquire position. The coordinates with the lowest horizontal dilution of precision is saved to memory.

The single frequency GPS can produce relatively noisy data and suffer from occasional data gaps. For the users' convenience,

© Author(s) 2025. CC BY 4.0 License.



Science Science Data

we distinguish between these direct GPS measurements, called gps_lat, gps_lon, gps_alt, and our best estimate of the station position at all time step, simply called lat, lon, alt derived in post-processing (see section 4.1).

2.1.12 Data logger and satellite modem (local data storage and transmissions)

CR1000X is a rugged, low-power data logger from Campbell Scientific, ideal for long-term monitoring in harsh environments. It offers faster processing, more memory, and improved analog precision compared to the CR1000, along with USB, RS-232, and Ethernet connectivity. These upgrades enhance data acquisition efficiency, reliability, and flexibility.

275

280

The NAL Research 9602-LP modem is a low-power, compact device designed for reliable long-range communication. It uses Iridium satellite connectivity, providing global coverage for data transmission. The modem supports Iridium Short Burst Data (SBD), which is a communication protocol designed for sending small amounts of data. It is optimized for low-bandwidth applications that need to transmit short bursts of data, such as sensor readings, GPS locations, or status updates. Iridium SBD enables reliable communication in areas without cellular coverage.

2.1.13 Batteries and solar panels (power)

We use two types of batteries for AWS power:

285

Lead-acid batteries are known for their ability to supply high surge currents, cost-effectiveness, and robustness in harsh environments (Table 2). Although their energy density is lower compared to more advanced battery chemistries, they offer consistent performance over a wide temperature range. In a controlled freezer test, we evaluated lead-acid battery performance and found that while charging below even -40°C is feasible, only a limited amount of energy is stored; nevertheless, they remain a reliable power source under extreme low temperatures.

Nickel-metal hydride (NiMH) batteries are also rechargeable but with higher energy density and reduced environmental impact compared to conventional lead-acid batteries. NiMH batteries exhibit relatively stable capacity across a range of temperatures; however, their performance becomes critically impaired at temperatures below -40 °C, where electrochemical activity ceases. In a series of controlled freezer tests, we evaluated NiMH battery performance at various subzero temperatures and confirmed that they remain a reliable power source down to approximately -40 °C.

295

For the reasons above, lead-acid batteries were chosen for high-elevation/far-North GC-NET sites at risk of temperatures below -40 °C, despite their lower energy density compared to the NiMH batteries.

300

RS PRO solar panels are high-efficiency photovoltaic modules designed to convert sunlight into electrical energy. These panels are made of either monocrystalline or polycrystalline silicon. RS PRO solar panels are known for their robust construction, suitable for harsh environments.



305

310



2.2 Automatic weather station design

The station designs differ between the ablation and accumulation areas due to variations in surface dynamics and logistical constraints. In the ablation area, the tripod stands on the ice and moves downward as the ice melts, keeping the sensor boom at a constant height above the surface. This design allows accurate surface-level measurements with only one sensor boom. During winter, temporary changes in surface height from snow accumulation are monitored using a sonic ranger mounted on the boom. In contrast, the accumulation area experiences continuous changes in surface height due to ongoing snowfall and snow compaction, making it harder to define a stable reference level. To accurately calculate meteorological gradients in this environment, a second measurement level is desirable. Additionally, practical considerations influence the designs: stations in the ablation area are often transported by helicopter, which often has limited cargo capacity, making compact, single-level setups preferable. In the accumulation area, larger two-level stations have been delivered by ski-equipped DHC-6 Twin Otter fixed-wing aircraft, which can carry bulkier equipment.

2.2.1 Accumulation area design: Mast with two measurement levels

The GC-NET mast configuration is a two-boom system, designed for accumulation area deployment. The two booms on the mast allow for vertical profiling of the near-surface boundary layer air temperature, wind speed & direction and humidity. The historical GC-NET mast configuration, originally deployed at 18 sites starting in 1995 as described in Steffen and Box (2001) and Vandecrux et al. (2023), consisted of a 4" diameter aluminum tube with a 1/4" wall thickness, providing a very stiff, but relatively heavy mast. Extending the mast thus required a tripod crane.

To enable a more light-weight system that would not require a crane, it was decided to investigate alternative mast solutions. The first light-weight alternative, deployed in 2021, was based on a 48 mm diameter titanium tube, fitted with two titanium booms. These tubes turned out to be too flexible for stable mounting of instruments, despite being anchored with 3 mm braided stainless-steel wires and reinforced with wooden poles inside. The second version, which has subsequently been deployed at all accumulation area sites, re-introduced the original outer mast diameter of 100 mm and aluminium, based on a combined analysis of weight, rigidity and usability of titanium, steel, aluminium and carbon fibre, respectively. To meet the weight requirements, the wall thickness of the 100 mm aluminium mast was reduced to 3 mm. Apart from reducing the weight of the mast itself, the number of the booms carrying the instruments were reduced from five to two, with the two booms positioned orthogonally, 1250 mm apart on the mast. Additionally, the choice of a more light-weight construction has enabled a field team of four to raise a fully instrumented mast without the use of a tripod crane and winch, further reducing the total weight to be carried on the airplane.

However, the light-weight construction has also required a positioning of instruments, solar panel and logger box that could potentially reduce the quality of the measurements, as they are more closely spaced than previously, increasing the risk of shading and turbulence. Similarly, the orthogonal position of the two booms provides different conditions for the two levels of

© Author(s) 2025. CC BY 4.0 License.



Science Science Data

wind measurements in terms of down-wind turbulence from the measurement frame. 335

Despite these potential issues, introducing a more light-weight mast structure has been deemed necessary in order to provide capacity for additional personnel (generally 4-6 people), regular transport of battery boxes, tools and replacement sensors, and equipment.

340

345

Fig. 2 illustrates the schematic of an accumulation area AWS, and Fig. 3 gives and in-situ impression from the field. Liquid precipitation is measured using a LUFFT WS401 sensor (1a), while humidity and temperature are recorded by a Vaisala sensor (1b). Visual- and infra light is measured by a CNR4 radiometer (2), which is equipped with with an integrated inclinometer/compass (2). Wind speed and direction are recorded by two anemometers (4), and snow height is measured by two sonic rangers (5). Power is supplied by a south-facing solar panel (6), connected to a battery box (9). Data acquisition and positioning are handled by a GPS and a logger box (7). Structural stability is ensured by an anti-torque rod (8) and a thermistor string (10) is drilled into the firn measuring temperatature at 11 different levels.

The standard accumulation area mast structure consists of 6 aluminium tube pieces as shown in Figs. 2 and 3:

350

- 1. A lower part with a plastic cup in the bottom, length 230 cm.
- 2. A middle part, referred to as the extension part, length 150 cm
- 3. An upper part where all instruments and boxes are attached to, length 220 cm
- 4. Two aluminium inserts as assembling parts, length 30 cm, outer diameter of 93.8 mm with a short length of 2 mm of slightly larger diameter where the mast pieces meet in the middle.

355

5. A one metre aluminium tube of similar type as the booms, fastened to the mast just below the snow surface at first installation to ensure that the mast does not rotate.

A mast and an insert are fastened using 3 rivets (5 mm) separated by 120 degrees. The accumulation area mast design makes it possible to always bring down the instruments for routine maintenance and rotation, without the use of a crane.

2.2.2 Ablation area design: Tripod with one measurement level

The AWS tripod is constructed using 32 mm (1.25 in) and 44 mm (1.75 in) diameter aluminum tubes, reinforced with 3 mm braided stainless-steel wires to form a stable tetrahedral structure (Figs. 4 and 5). Most sensors are mounted on a 1.7 m long horizontal boom positioned 2.7 m above the surface (Fig. 4). To enhance stability, a battery box weighing approximately 50 kg is suspended beneath the mast on wire ropes with shackles, lowering the centre of gravity of the AWS installation. The tripod design allows it to be folded for transport in small helicopters and tilted for sensor replacements.



375

380

385

395



The sensor housing with thermometer and hygrometer is located approximately 2.6 m above the ice surface (i.e. as high as possible underneath the sensor boom). The measurement height varies when a winter snow cover is present (Fig. 4, item 1). The inclinometer is mounted on the sensor boom (Fig. 4, item 2) and aligned with the radiometer to allow for tilt correction in shortwave radiation measurements. Compared to Fausto et al. (2021), the inclinometer and compass are integrated into the CNR4 radiometer for improved alignment. The radiometer is installed as an extension of the boom and faces south, as shown in Figs. 4 and 5. In the latest AWS designs, the compass also provides orientation data to record any rotation of the boom or tripod. The wind sensor is mounted on the opposite side of the boom from the radiometer (Fig. 4, item 4), measuring approximately 40 cm above the boom. The sonic ranger is mounted on the boom directly under the wind sensor with a distance to the ice surface of approximately 2.6 m (Fig. 4, item 5), while the SR50A mounted on a stake is drilled into the ice and melts out with the ablating ice surface during summer (Fig. 4, item 12). As the tripod rests freely on the ice surface, it moves down as the ice melts, meaning the sonic ranger measurements on the AWS do not capture ice melt, only snowfall and snowmelt. The separate sonic ranger on the stake (8 m), constructed from 40 mm carbon fibre tubing and typically drilled 6-7 m into the ice, does record any sort of accumulation and ablation (Fig. 4). In addition to sensor-related uncertainties, occasional complications arise when a stake assembly melts out and falls over. The data logger enclosure also includes the Iridium modem and GPS receiver. A single-frequency GPS receiver is used to measure the position and elevation of each station to determine e.g. ice flow velocity (Figure 4, item 7). The Iridium antenna is mounted on the boom (Figure 4, item 3) to ensure optimal satellite reception. The PTA bladder box (Fig. 4, items 8 and 10) is mounted on the mast approximately 1.5 meters above the ice surface, with any spare or melted-out hose resting on the surface and the remaining hose drilled into the ice, measuring ice melt. Fig. 4 illustrates the free-standing AWS tripod, which moves downward as the ice surface ablates, while the hose itself melts out of the ice. This process reduces the hydrostatic pressure exerted by the liquid column over the transducer, allowing direct calculation of ice ablation. The power system includes rechargeable batteries connected to a relatively small solar panel without a charge controller. (Fig. 4, items 6 and 9). The solar panel is mounted on the mast, facing south, and positioned well above the ice surface to prevent winter snow accumulation from covering the panel. The thermistor string (Fig. 4, item 11) is drilled 10 m into the ice.

All stations on bedrock uses the tripod setup without a pressure transducer assembly, a thermistor string, and a stake assembly.

AWS KAN_B additionally includes a rain gauge of type Geonor T200B for precipitation measurement.

2.3 Site-Specific Merging of Data from Multiple Stations

We distinguish between "station" and "site", where station is one specific AWS and site is a location that may encompass data from more than one AWS (Table 3). The difference between station and site is as follows:

The term "station" refers to a coherent AWS installation. A given station can sometimes be upgraded (instruments, datalogger, etc.) or relocated. Vandecrux et al. (2023) define GC-NET AWS data collected before the GEUS takeover as "historical data", which they revisited by removing errors and applying quality adjustments to meet higher standards. This effort ensured compatibility between historical records and data from present-day accumulation-area stations. New ablation-area tripod stations,

© Author(s) 2025. CC BY 4.0 License.



405

420

425

Science Science Data

400 initially labeled "v3" to replace decommissioned "v2" models, have been installed at most sites. As a result, multiple stations at a given site can now be consolidated into a single site-specific dataset.

The term "sites" refers to locations with a radius of less than 4 km where one or more stations are, or have been, operational. For simplicity, each site is named and recorded as site_id in the data file attributes. For example, the site QAS_U includes data from both the QAS_U and QAS_Uv3 stations, while the site SDM includes data from the historical South Dome station and the current SDM station. Nearby stations can be active simultaneously, producing redundant observations at a given site. The complete list of sites is provided in Table 3 and see Fig. 1 for examples.

In the updated, PROMICE | GC-Net data product, the distributed files are site-specific. The list of the 52 sites and the names of distinct stations that are currently grouped under each site appears in Table 3.

2.4 Measurements and data transmissions

Measurements are taken every 10 minutes and stored in the data logger. For most measured variables, the logger converts voltage readings into physical values using simple scaling relations based on calibration coefficients specific to each instrument. In cases where identical sensors may have different calibration coefficients, such as the radiometer and pressure transducer, voltage is converted using automatic procedures (to be described in section 3). This approach allows sensor replacements without requiring changes to the logger program.

The AWSs transmit hourly averages based on measurements occurring every ten minutes year round. Older AWS versions (Fausto et al., 2021) transmit hourly averages between day of the year 100 and 300 (10 April and 26 October in non-leap years). Parameters that do not have significant sub-daily changes (GPS position, station tilt, surface height, etc.) are transmitted less frequently (every 6 h) to reduce the transmission cost. In winter, between day of the year 300 and 100, the previous AWS versions transmitted daily averages of all parameters to limit power consumption by the satellite modem when little solar charging was available. Transmission is done through the Iridium satellite network that has coverage even at the northernmost latitudes. The Iridium Short Burst Data service transmits up to 340 bytes per message. The logger program ensures successful data transmission by implementing a message queue to handle situations where the Iridium satellites are unavailable. This relatively low-power operation mode ensures unnecessary transmission attempts with a low rate of message loss. Moreover, the logger program encodes the data in a binary format before transmission, which reduces the size of the message, thereby reducing transmission costs by about two-thirds.

2.5 AWS maintenance

430 To ensure reliable and accurate measurements, instruments in the field are replaced according to a maintenance schedule informed by manufacturer recommendations and operational experience, such as battery life and performance when charging without a charge regulator. This schedule serves as a guideline, but field crews cannot always return to an AWS in time to

© Author(s) 2025. CC BY 4.0 License.



Science Science Data

perform a scheduled sensor swap (Table 2). For instance, the AWSs in northeastern Greenland (KPC; Fig. 1) are visited only every 3–4 years due to their remote location. Fortunately, these remote AWSs experience less melt, lower accumulation, and less severe storms compared to several other regions, so that some aspects of the maintenance visits become less urgent.

Maintenance visits at ablation sites (tripod type on ice) are typically performed by two people and last 2–4 hours, carrying out data download from the logger, documenting the state of the AWS, replacing sensors scheduled for recalibration, re-drilling the PTA, thermistor string and sonic ranger stake in ice, and conducting any necessary repairs.

440

Maintenance visits at accumulation sites (mast type in snow/firn) are typically performed by a core team of four people, last 3–7 hours, and often involves assistance from further personnel, e.g., helicopter or aircraft crew. Apart from data download and instrument replacement, maintenance visits at accumulation sites include:

- Extending the mast to counter snow accumulation.
- Digging out and raising the battery box.
 - Retrieving a snow pit density and snow temperature profile at 10 cm vertical resolution, covering the snow accumulated since the last visit.
 - Drilling a 10 m firn core for density profiling at core breaks and stratigraphic characterization.
 - Measuring and repositioning a snow stake fitted with a board to mark the time of maintenance visit.
- 450 Performing a GNSS survey of the mast position and elevation.

For the thermistor string, the cable (including the cap) connecting the thermistor system with the AWS is detached and replaced (it is buried deep in snow) and an additional 2 m polypropylene pipe is added, while the entire thermistor string is carefully pulled up to reposition the top thermistor at the surface level.

Further measurements at accumulation sites have included radar surveys of snow depth and snow micro-penetrometer measurements (Schneebeli et al., 1999). The aim is to visit all the accumulation sites annually, but occasionally, AWS's in low-accumulation areas are visited biannually, unless instruments require maintenance or replacement.

3 Data product

This section details the data processing pipeline, including filtering, measurement corrections, and the derivation of variables, as well as the computation of hourly, daily, and monthly averages. The following sections also describe the AWS dataset contents, variable definitions, data types, and key differences in processing for ablation- and accumulation-area stations. Together, these sections present the new and updated AWS dataset.



485



3.1 Data Processing Pipeline

Here, we use the data processing pipeline called "pypromice". pypromice is the open-source Python library used for processing raw AWS data in Greenland (How et al., 2023a, b). It provides tools for importing, cleaning, and quality-controlling raw AWS measurements, computing derived meteorological variables such as surface temperature, and performing temporal aggregation and visualization. pypromice enables researchers to efficiently work with large AWS datasets, reproduce analyses, and integrate AWS observations with other datasets.

- 470 The processing pipeline is structured around two operational components and two key data inputs (Fig. 6):
 - Active AWS deployments: Each AWS logs 10-minute data locally and transmits hourly measurements via Iridium. The
 complete set of 10-minute data files are retrieved and ingested into the pipeline after maintenance visits.
 - pypromice: This is the central processing component responsible for fetching, processing, and publishing data from all active AWS; documented in How et al. (2023b).
- QC flags and adjustments repository: Manual quality control is managed via the public GitHub repository "PROMICE-AWS-data-issues", serving as a collaborative space for data review and external feedback.
 - **Historical GC-Net dataset:** A pre-processed dataset containing historical data from the GC-Net network (Vandecrux et al., 2023) is used as an additional data input to obtain long-term time series for sites.

The AWS data pipeline organizes the dataset into four hierarchical processing levels (Fig. 7). Each level represents a distinct stage in the transformation and validation of the data, from raw logger output to finalised quality-controlled datasets with a selection of transformed and derived variables.

- Level 0 (L0): Holds the raw data as recorded by the station data loggers. These measurements are collected either via Iridium transmissions or during field visits and remain uncalibrated. As logger configurations vary between stations, so do the formats, variables, and sampling frequencies. Level 0 serves as an immutable source layer from which all further processing is derived.
- Level 1 (L1): Converts raw measurements into physically meaningful units and standardizes the dataset across stations. This involves applying calibrations, decoding sensor outputs, and adopting a consistent variable naming scheme, resulting in a unified and interpretable data structure.
- Level 2 (L2): Adds quality control and initial physical interpretation. It incorporates both manual corrections and automated checks, applies filters to remove or correct suspect values, and computes selected derived variables such as cloud cover, albedo, and corrected radiation measurements.

© Author(s) 2025. CC BY 4.0 License.



Science Science Data

- Level 3 (L3): Synthesizes the processed data into a set of derived variables suitable for research applications. This includes turbulent heat fluxes, continuous surface and snow height records, time-dependent station positions, and other higher-level outputs required for e.g., energy and surface mass balance studies.

In addition to the processing levels, the pipeline defines a set of core concepts for modelling time and space. A *station* refers to a specific version of an AWS for a specific location, covering both tripod and mast stations. The configuration and instruments of the station can change over time due to maintenance visits. Periods with a fixed setup are treated as individual L0 data files, ensuring consistency with related parameters such as calibration coefficients. A *site* is an area that may include multiple stations. As described in Section 2.3, station data can be aggregated into sites to produce longer time series.

500 3.1.1 Data Acquisition

There are multiple types of L0 data collected from the AWS data loggers, while the formats can vary depending on local installations and logger programs.

- Raw data: Recorded every 10 minutes and retrieved from the data logger during maintenance visits. This can either be retrieved directly from the memory card or downloaded from the data logger.
- SlimTable: A format used by older AWS as a lighter hourly aggregated raw format due to limited logger memory.
 - Transmission data: Collected on an hourly basis and includes a subset of the variables from the latest record.

The pipeline supports all formats with raw data, when available, in favour of transmissions. Transmissions cover the period since the latest visit and serve as a fallback in case of missing or corrupted raw data. New transmission data is processed in near-real-time every hour, with a latency of approximately five minutes between transmission and production-ready data.

510 3.1.2 pypromice

505

515

520

AWS data are processed by the pypromice Python package (https://github.com/GEUS-Glaciology-and-Climate/pypromice) (version 1.5.1), a peer-reviewed suite of algorithms in a standardised workflow for transforming original AWS data (hereafter referred to as L0) to a processed, finalised, user-ready L3 data product (How et al., 2023a) (Fig. 7). The pypromice package is available via pypi and conda-forge for easy deployment and contains full-coverage unit testing to ensure continuous integration and compatibility across versions and updates.

3.1.3 Dataset Variables: Derived and Corrected Variables

This section provides an overview of the derived and corrected variables included in the dataset. It outlines the calculations used to generate these variables and presents them in a structured dataset variables table. Methods for deriving new variables or correcting existing ones are described, ensuring transparency and reproducibility of the data processing steps. In the available netcdf files, the long variable names and a dedicated attribute indicate whether a variable is a direct measurement or calculated





in post-processing. This metadata is also summarized in a CSV file "variable.csv" distributed along with the data (How et al., 2022a).

Specific humidity

The specific humidity q (in kg kg⁻¹) is calculated from the relative humidity RH (with respect to water or ice, depending on the temperature) using the following equations:

$$q = \frac{RH}{100} \cdot q_{\text{sat}},\tag{6}$$

where

535

540

545

$$q_{\text{sat}} = \frac{\varepsilon e_{\text{sat}}}{p - (1 - \varepsilon) e_{\text{sat}}}.$$
 (7)

In these equations, $\varepsilon = 0.622$ is the ratio of the specific gas constants for dry air and water vapor, p is the air pressure (in Pa), and e_{sat} is the saturation water vapor pressure (in Pa) over either ice (for below freezing) or water (for above freezing), as calculated following Goff and Gratch (1946).

Surface temperature

The surface temperature T_s (in °C) is calculated using Stefan–Boltzmann law by using the measured downward and upward longwave irradiance (LR_{in} and LR_{out} , respectively) with the following equation:

$$T_s = \left(\frac{LR_{\text{out}} - (1 - \varepsilon)LR_{\text{in}}}{\varepsilon \cdot 5.67 \times 10^{-8}}\right)^{0.25} - T_0,\tag{8}$$

where the ice sheet surface emissivity is assumed to be $\varepsilon = 0.97$ and $T_0 = 273.15$ K.

Turbulent energy fluxes

With key surface meteorological values known, such as temperature from longwave radiation, saturated humidity, and zero wind, turbulent heat flux gradients can be calculated without a second sensor boom. The sensible heat flux (SHF) and latent heat flux (LHF), expressed in (W m⁻²), are estimated from vertical gradients in wind speed, potential temperature, and specific humidity between the instrumented boom height and the surface, following the method described by Van As et al. (2005); Van As (2011). Based on Monin–Obukhov similarity theory, SHF and LHF are approximated as:

$$SHF = \rho C_p \kappa^2 \frac{u}{\ln \frac{z_u}{z_0} - \psi_u} \frac{T - T_s}{\ln \frac{z_T}{z_{0,T}} - \psi_T},\tag{9}$$

$$LHF = \rho L_{s/v} \kappa^2 \frac{u}{\ln \frac{z_u}{z_0} - \psi_u} \frac{q - q_s}{\ln \frac{z_q}{z_{0,q}} - \psi_q},$$
(10)

where ρ denotes the air density, and $C_p = 1005 \, \mathrm{J \, K^{-1} \, kg^{-1}}$ is the specific heat capacity of air at constant pressure. The latent heat of sublimation and evaporation are $L_s = 2.83 \times 10^6 \, \mathrm{J \, kg^{-1}}$ and $L_v = 2.50 \times 10^6 \, \mathrm{J \, kg^{-1}}$, respectively. The von Kármán constant is $\kappa = 0.4$. Positive fluxes contribute energy to the surface, whereas negative fluxes withdraw energy from it.

© Author(s) 2025. CC BY 4.0 License.



560

565

575



To estimate turbulent heat fluxes, we require measurements of the following variables at given heights: wind speed (z_u) , temperature (z_T) , and specific humidity (z_q) . Additionally, we need the surface roughness lengths for momentum (z_0) , heat $(z_{0,T})$, and moisture $(z_{0,q})$. A constant value of $z_0 = 0.001$ m is used, while $z_{0,T} = z_{0,q}$ is calculated based on the formulation for rough surfaces by Smeets and Van den Broeke (2008a, b). Atmospheric stability corrections are applied using the functions $\psi_{u,T,q}$ from Holtslag and De Bruin (1988) for stable conditions and from Paulson (1970) for unstable conditions. Surface temperature (T_s) is derived from longwave radiation (see Eq. 8), and the surface specific humidity is assumed to be at saturation, i.e., $q_s = q_{\text{sat}}$.

Several sources of uncertainty affect the calculation of sensible (SHF) and latent heat fluxes (LHF). The aerodynamic surface roughness length z_0 varies with surface type (Brock et al., 2006) and over time (Smeets and Van den Broeke, 2008a, b). Assuming a constant value of $z_0 = 0.001$ m may overestimate surface roughness in snowy conditions and thus lead to overestimations of both turbulent fluxes.

Box and Steffen (2001) showed that one- and two-level methods underestimate downward latent heat flux under extreme stability. Miller et al. (2017) found similar biases in sensible heat flux, with one-level methods offering longer records. Fausto et al. (2016a, b) highlighted the use of unrealistically high surface roughness lengths (z_0) to match surface energy balance closure with melt-driven ablation rates during intense heat flux events. Turbulent heat flux estimates over ice and snow are uncertain due to assumptions of surface homogeneity, stable polar boundary layers limiting turbulence, surface variability, scarce measurements, and sensitivity to temperature errors. Thus, these estimates require cautious interpretation.

Tilt correction of downward shortwave radiation

Tilt correction of solar radiation follows the method outlined by Van As (2011), which is also described by Fausto et al. (2021). Downward shortwave radiation ($SR_{\rm in}$) is composed of both diffuse and direct beam components, but only the direct beam component requires correction for surface tilt. For a horizontal radiation sensor, the direct beam component, equivalent to $SR_{\rm in}$, is reduced by the diffuse fraction ($f_{\rm dif}$). For a tilted sensor, $SR_{\rm in}$ is derived from the measured radiation ($SR_{\rm in,m}$) using a correction factor C, as follows:

$$SR_{in,cor} = SR_{in,m} \frac{C}{1 - f_{dif} + Cf_{dif}},\tag{11}$$





with

580

585

$$C = \cos(SZA) \cdot \left(\sin(d)\sin(lat)\cos(\phi_{sensor}) - \sin(d)\cos(lat)\sin(\theta_{sensor})\cos(\phi_{sensor}) + \cos(d)\cos(lat)\cos(\theta_{sensor})\cos(w) + \cos(d)\sin(lat)\sin(\theta_{sensor})\cos(\phi_{sensor})\cos(w) + \cos(d)\sin(lat)\sin(\theta_{sensor})\cos(\phi_{sensor})\cos(w) + \cos(d)\sin((\theta_{sensor})\sin(\phi_{sensor})\sin(w) \right)^{-1},$$

$$(12)$$

where SZA is the solar zenith angle, d is the solar declination (the angle between the Sun and the Earth's equatorial plane), ω is the hour angle (the angular distance between the Sun's current position and solar noon), lat is the site's latitude in radians, and θ_{sensor} and ϕ_{sensor} represent the radiometer's tilt angle and azimuth orientation, respectively. The procedures for calculating d (solar declination), ω (hour angle), and SZA (solar zenith angle) are found in Fausto et al. (2021). Table 5 presents the average bias or correction applied to incoming solar radiation based on Equation 11. For most AWS stations, the standard deviation shows that the average correction is small, typically less than $15\,\mathrm{W\,m^{-2}}$, although a few stations exhibit a broader range of correction values. We estimate the diffuse fraction (f_{dif}) to range from 0.2 under clear-sky conditions to 1.0 during overcast skies, assuming a linear relationship with cloud cover fraction, as described by Harrison et al. (2008).

Cloud cover

To approximate the cloud cover fraction, we rely on the relationship between near-surface air temperature (T_{air}) and downward longwave radiation (LR_{in}), following Van As et al. (2005). Specifically, we compute the theoretical clear-sky downward longwave radiation flux using the formula proposed by Swinbank (1963):

$$LR_{clear} = 5.31 \cdot 10^{-14} \cdot (T_{air} + T_0)^6, \tag{13}$$

where LR_{clear} is the clear-sky longwave radiation flux (in W m⁻²) and T_{air} is the near-surface air temperature (in Kelvin). This allows us to estimate the cloud cover fraction by comparing observed longwave radiation to the clear-sky baseline.

Theoretical downward longwave radiation under overcast conditions is estimated by assuming black-body emission from a cloud base at the near-surface air temperature. This is calculated using the Stefan–Boltzmann law:

$$LR_{overcast} = 5.67 \cdot 10^{-8} \cdot (T_{air} + T_0)^4, \tag{14}$$

600 where LR_{overcast} is the overcast longwave radiation flux (in W m⁻²), T_{air} is the near-surface air temperature (in °C), and T_0 is the conversion offset to Kelvin (273.15 K).

The cloud cover fraction (cc), constrained within the range [0,1], is then estimated by linearly scaling the observed longwave radiation between clear-sky and overcast conditions:

$$cc = \frac{LR_{in} - LR_{clear}}{LR_{overcast} - LR_{clear}} = \frac{f_{dif} - 0.2}{0.8}.$$
(15)





The cloud cover estimation is only valid over ice and snow surfaces, and therefore is not computed for stations installed on bedrock.

Albedo

610

615

620

625

630

Surface broadband solar reflectivity in the 0.3– $2.5\,\mu m$ wavelength range, commonly referred to as albedo (unitless), is derived from 10-minute tilt-corrected measurements of downward and upward solar irradiance. Hourly albedo values are computed when the solar zenith angle is under 70° (i.e., when the sun is more than 20° above the horizon), ensuring optimal measurement reliability for the pyranometer. Daily mean albedo values are then calculated from the valid hourly data. Shadows cast by AWS components, such as the mast or sensor arms, together with surface contrast with AWS infrastructure (e.g., solar panel, battery box, legs, enclosure), and the presence of features such as melt ponds beneath the station can reduce observed albedo values by up to 0.03 on average, depending on surface type and snow surface height (Kokhanovsky et al., 2020). This bias source is variable with snow surface height, effectively zero when snow thickness exceeds 1.5 m. Ryan et al. (2017) compared ablation area AWS albedo measurements with unmanned aerial vehicle (UAV)-derived and satellite-based albedo products, finding increasing discrepancies during the late melt season due to spatial inhomogeneity and limited representativeness of point measurements. While van den Broeke et al. (2004) reported a 5% uncertainty for pyranometer-based albedo measurements, the instrument manufacturer (Kipp & Zonen) suggests a more conservative estimate of 10%, adopted here for the calculated albedo values.

Ice surface height

The pressure transducer assembly (PTA; Fig. 4) is sensitive to fluctuations in atmospheric pressure, which can influence the measured signal H_M . To correct for this effect, the contribution of air pressure is removed using the following expression:

$$H_L = H_M + \frac{P_C - P_A}{g\rho_l},\tag{16}$$

where P_A (in hPa) represents the ambient air pressure, while P_C (in hPa) is the reference pressure specified by the manufacturer during sensor calibration. The gravitational acceleration is assumed to be $g=9.82\,\mathrm{m\,s^{-2}}$, and the density of the antifreeze mixture used in the system is $\rho_l=1090\,\mathrm{kg\,m^{-3}}$, for a temperature of $0\,^\circ\mathrm{C}$. Cumulative variations in the corrected liquid level H_L directly correspond to ice surface ablation. Fausto et al. (2012, 2016a) validated PTA-derived ablation measurements against manual hose-based readings and sonic ranger data, and found the PTA measurements to be accurate within $\pm 0.04\,\mathrm{m}$.

Precipitation correction

Following Box et al. (2023), we correct precipitation measurements for undercatch using wind speed (U). We apply the undercatch correction factor (k) for an unshielded Hellmann-type gauge under liquid-only precipitation conditions, using the catch-efficiency relation from Yang et al. (1999):

$$k = \frac{100}{100 - 4.37U + 0.35U^2},\tag{17}$$





where U is wind speed (in m s⁻¹) at measurement height. The correction was originally derived from daily mean wind speeds up to 6.5 ms^{-1} , but is assumed to be applicable to hourly wind speed data. For wind speeds exceeding 6.5 ms^{-1} , an extrapolated correction is applied (Yang et al., 1999). As with all automated precipitation measurements, considerable uncertainty persists in the corrected values, as wind speed alone does not fully account for the observed undercatch.

640

645

Moreover, only rainfall is considered in this undercatch correction by excluding measurement periods where air temperature is below -2 °C. However, this does not eliminate the affect of delayed snow melt errors, when snow accumulates in the gauge and is only registered as precipitation as it melts into the tipping bucket. Such instances can occur during short atmospheric warm spells within otherwise sustained below-freezing conditions during winter. As a result, corrected rainfall should be used and interpreted with caution.

3.2 Dataset structure

Multiple versions of the AWS datasets are available, reflecting different processing levels, temporal resolutions, and aggregation scales (station vs. site):

- L2: Station data, hourly
- **L3:** Site data, hourly, daily, and monthly

The L2 datasets are quality-controlled and noise-filtered. This is the least processed public product, closely reflecting the original station measurements. The L3 datasets are the highest level of processed data, including derived variables, and is documented in Section 3.2.2. The L3 product is provided only at the site level, enabling the creation of longer, continuous time series.

655 3.2.1 Metadata and Data Discoverability Attributes

The datasets are distributed with a comprehensive set of metadata, following the Climate and Forecast (CF, Hassell et al. (2017)) conventions and the Attribute Convention for Data Discovery (ACDD). In addition, specific attributes are included to capture station- and site-levels details relevant for interpretation, reuse and reproducibility. For example, the specific attribute site_type is added to describe the environment type of the installation site (e.g., ablation, accumulation, or tundra).

660 3.2.2 Data variables

665

The data variables are CF-compliant according to CF-1.7 and use an updated naming convention relative to our earlier products. The L3 hourly datasets contain a full set of data variables from our processing pipeline and are summarised in Table 4. Many variables are measured at both the upper and lower boom in cases where stations or sites follow the accumulation area two-boom station design. In addition, instantaneous measurements are provided for key variables (air temperature, air pressure, relative humidity, wind speed, and wind direction), whereby instantaneous measurements are recorded at the top of each hour.





For stations or sites with the ablation area one-boom station design, variables are assigned as upper boom measurements, with no corresponding lower boom values provided.

3.2.3 File formats

The datasets are provided in both NetCDF and CSV formats. The data itself is unchanged between these two versions, however, the NetCDF format includes metadata and variable attributes which better inform about the collection and quality of the data. We therefore recommend users adopt the NetCDF format where possible.

3.3 Quality Control and Filtering Routines

The transformation from L1 to L2 introduces quality control mechanisms. This includes the application of automated filters as well as the integration of manual flags and adjustments maintained in the public repository:

675 https://github.com/GEUS-Glaciology-and-Climate/PROMICE-AWS-data-issues.

Four stringent filtering routines are adopted in the production workflow to remove erroneous data and outliers. These filtering routines are performed and included in the L2 dataset (i.e., performed between L1 and L2).

3.3.1 Physical and sensor specific thresholds

An upper and lower threshold is adopted to filter out erroneous measurements. These thresholds are informed by the instrument upper and lower measurement capabilities, commonly documented by the instrument manufacturers (See Appendix).

3.3.2 Percentile filtering

To detect outliers while preserving natural variability, a percentile-based filtering method is applied to selected variables for each individual station. This method uses the stations-specific 5th and 95th percentiles, adjusted by predefined offsets, to define acceptable value ranges (Table 6).

685

690

For air temperature, thresholds are computed separately for four seasons to account for seasonal variations (Fig. 8). For other variables, a single year-round threshold is used. These thresholds are computed individually for each station, based on historical data, to account for site-specific conditions and distributions. Figs 8 and 9 illustrate the resulting thresholds for air temperature and pressure for the AWS station NUK_U. As an example, air temperature measurements at NUK_U follow seasonal trends, and the four-season thresholds (dashed lines) capture this behavior. However, a noticeable shift upwards in 2021 is visible, where values approach or exceed the upper threshold. This is due to a failure of the aspiration fan, which caused the sensor to heat up in sunlight and record artificially high temperatures.

For pressure, static thresholds are applied across all years. While generally effective, some valid measurements are falsely

© Author(s) 2025. CC BY 4.0 License.



Science Science Data

flagged as outliers, particularly during low-pressure weather events, highlighting a limitation of using fixed thresholds for inherently variable parameters.

3.3.3 Persistence

To detect sensor or data logging malfunctions that result in unchanging measurements, a persistence-based filter is applied as part of the quality control. This filter is designed to identify and flag periods where values remain constant over time, a typical symptom of readout failures or stuck sensors. Persistence filtering targets a known behavior of some logger programs: when a sensor readout fails, the system may fall back to returning the last successfully measured value. If the issue persists, the output becomes artificially constant for hours or days. Fig. 10 shows an example of persistent relative humidity readings from station CP1 in January 2022. The red line shows the values before the persistence filter and black line shows after.

3.3.4 Manual filtering and adjustments

Manual intervention is sometimes required where it is known that the data does not reflect true conditions at the station. Measurements can be untrue representations of conditions during station maintenance visits, for example, if a station needs to be tilted or moved. In these cases, data can either be flagged and therefore removed from the dataset; or adjusted using a predefined set of supported operators.

Manual quality control is implemented as an asynchronous and collaborative process based on a public GitHub repository https://github.com/GEUS-Glaciology-and-Climate/PROMICE-AWS-data-issues that allows both internal and external users to contribute by either raising a data issue here, or proposing their own adjustments to the dataset. This is reviewed by a member of the PROMICE | GC-NET AWS data team. Flagging and adjustment rules defined in this repository are integrated into the pypromice production pipeline, where they are applied to the data products on an hourly basis.

715 3.4 Temporal resolution and success rate

The temporal resolution of AWS data depends on several factors, including the logger program version, data source, measured variable, season, and the operational status of the station. Three primary types of data tables are generated:

- Raw data tables (Raw) contain instantaneous samples with the highest available temporal resolution (10 minutes), collected during maintenance visits.
- Slim Table Memory (STM) is a compact dataset used in some older CR1000 logger programs. It stores hourly averaged values as an internal backup to maximize storage capacity during long deployments while preserving essential measurements.

© Author(s) 2025. CC BY 4.0 License.



725

Science Science Data

- Transmitted data tables (TX) are sent via Iridium including hourly averaged values typically combined with selected instantaneous measurements for real-time use by meteorological offices. Averages are timestamped at the end of each period by the data logger. See Section 3.4 for more information on transmissions.

The processing pipeline is built around hourly averaged measurements, which are standardized to use timestamps at the beginning of each averaging period. In addition, hourly instantaneous values are preserved in separate variables for meteorological analyses, while the higher-frequency raw (10-minute) data are primarily used for aggregation and sensor-specific corrections.

Fach published AWS dataset is distributed as an hourly sampled time series, which forms the primary product. For user convenience, aggregated daily and monthly datasets are also provided. However, we recommend that users rely on the hourly data when performing further analysis or custom aggregations.

Hourly averages are computed from 10-minute values when at least 80% of the data are available. Daily averages are then derived from hourly averages, also requiring at least 80% data availability for variables exhibiting clear diurnal variability. For less transient variables, a single measurement is sufficient to compute an average. Finally, monthly averages are calculated from daily averages when at least 80% of the data are present.

3.4.1 Success rate for key measurements

Using the daily data product, AWS data coverage was assessed using a 'success rate', defined as the ratio of days with valid daily averages for all variables required to estimate the surface energy budget (air pressure, air temperature, humidity, wind speed, and downward and upward shortwave and longwave radiation) to the total days since AWS installation. Performance for these critical variables by site and measurement period is shown in Fig. 11. The historical GC-NET dataset lacks full surface energy balance coverage due to differing instrumentation from all accumulation area stations (Vandecrux et al., 2023).

4 Post-processing

This section outlines the key L2 to L3 post-processing steps applied to the dataset to ensure data consistency, accuracy, and usability. Section 4.1 provides the displacements of Automatic Weather Stations (AWS), summarized in a dedicated table. Section 4.2 describes the AWS reposition history. Section 4.3 describes methods used to estimate surface height from multiple sensors, supported by illustrations. Section 4.4 covers how thermistor depth is estimated and how 10-meter ice or firn temperatures are calculated. Lastly, Section 4.5 presents visual examples of representative datasets to illustrate the data product.

750 4.1 Time-dependent AWS position data

The AWS on ice are displaced over time by ice flow and surface ablation. The single-phase GPS available on all active stations provides relatively noisy data and occasionally has gaps. To provide continuous coordinates, we fit piecewise linear functions to the available GPS measurements and derive gap-free, smoothed positions for all timestamps. A discontinuity is introduced

© Author(s) 2025. CC BY 4.0 License.



760

775

780

Science Science Data

in these smoothed coordinates whenever the station is repositioned. An overview of the station displacements are provided in Table 7 and details on station repositioning during maintenance visit are provided in section 4.2.

Historical GC-Net stations did not record continuous GPS positions. To address this, Vandecrux et al. (2023) compiled handheld GPS measurements and GNSS surveys collected during maintenance visits. For stations showing significant displacement and with sufficient point measurements, latitude and longitude were linearly interpolated. Sites with no position data (JAR2/JR2 and JR3), and sites with minimal vertical and horizontal displacement (less than approximately 10 meters), such as Summit (SUM), SDL, SDM, NEM, and NGRIP (NGP), are represented by constant latitude, longitude, and elevation values.

To represent elevation changes at historical GC-Net sites, which are important for applications such as barometric data assimilation in reanalysis, the time-dependent elevation of pre-GPS AWS data has been reconstructed using a combination of the following sources:

- 1. NASA Airborne Topographic Mapper (ATM) data beginning in 1993 (Thomas and Studinger, 2010; Studinger, 2014), within a 1 km horizontal search radius from daily horizontal position data (see Fig. 15),
- 2. Monthly satellite altimetry from 2003 to 2023 (Khan et al., 2025), for annually varying latitude and longitude,
- 3. A selection of handheld GPS measurements (see Table 7) (Vandecrux et al., 2023),
- 4. Monthly averaged GEUS carry-forward GC-Net onboard GPS data since 2020, in the case of Swiss Camp,
 - 5. Repeat geodetic surveys from 1991 to 2022 for Swiss Camp and JAR (Stober et al., 2023).

Fig. 15 illustrates the approach, where a linear function is fitted to the various elevation observations and interpolated temporally between points represented by magenta line. Only at Swiss Camp and JAR was it necessary to place multiple temporal interpolation points due to multi-year variability in site elevation caused by dynamic thickness changes. At other sites, a single linear temporal function was sufficient.

4.2 AWS reposition history

To date, stations JAR, KAN_L, NUK_L, NUK_U, QAS_L, QAS_M, SWC, and THU_U have been relocated during maintenance by distances exceeding 90 m horizontally (Table 8). Site repositioning has, for example, been carried out to avoid crevassed areas as in the case of the first year of QAS_L data or to mitigate recurrent station damage caused by excessive snowfall accumulation, as observed during the initial years at QAS_M. The Swiss Camp station, that had moved 4 km down glacier between 1990 and 2022, was replaced by the SWC_O station installed near (2.5 km north of) the 1990 position.

A total of 4,961 hours of concurrent data from the SWC and SWC_O stations, located 5.9 km apart, allowed for evaluating differences to test the assumption that the measurements represent a single site. Air temperature showed no significant



800



difference, with a mean offset of 0.2 ± 0.6 °C. Surface air pressure differed by an insignificant 4.8 ± 4.8 hPa, and wind speed differed by 1.1 ± 1.6 m s⁻¹.

4.3 Surface Height Estimation from Multiple Sensors

Surface height is measured using multiple instruments. In this update, a new L3 variable, "z_surf_combined", integrates data from several sensors to provide a continuous record of surface elevation, except during periods when all surface-ranging instruments fail. This variable also supports the estimation of time-varying thermistor depths used for subsurface temperature measurements (see section 4.4). The method builds on approaches previously applied in scientific studies (Vandecrux et al., 2024).

At accumulation sites, surface height is derived from two sonic rangers mounted on the station booms. After correcting for height jumps caused by maintenance or mast adjustments, the two measurements are averaged to form z_surf_combined, reducing the influence of tilt, noise, and limited spatial coverage.

Tripod stations are equipped with three instruments:

- A sonic ranger mounted on the station,
- A sonic ranger mounted on a separate stake assembly,
- A pressure transducer installed in a borehole within an ablation hose (Fausto et al., 2012).

The station-mounted sonic ranger detects snow accumulation but cannot measure ice surface lowering during ablation, as the station descends with the ice. The stake-mounted ranger captures both snow accumulation and ice melt. Sonic ranger data are cleaned of errors, corrected for air temperature sensitivity where possible, converted to surface height, and adjusted to remove jumps from stake maintenance. The pressure transducer records only ice surface lowering and is unaffected by snow accumulation.

To construct z_surf_combined, the following procedure is applied:

- z_ice_surf is derived from z_pt_cor and manually adjusted after maintenance to ensure continuity.
- The ablation period is defined annually as the interval between the first and last weeks where z_ice_surf decreases. If unavailable, June-August is used.
 - During ablation, z_surf_combined equals z_ice_surf, unless missing, in which case the stake-mounted ranger is used.
 - At the end of ablation, sonic ranger readings are aligned with z_ice_surf, enabling snow accumulation tracking during winter.

© Author(s) 2025. CC BY 4.0 License.



825

830



- During the snow season, z_surf_combined is the average of the two sonic ranger measurements.
 - In spring, as snow melts, surface height declines until it matches the ice surface height from the previous ablation season.
 From this point, the pressure transducer data are again used.

This procedure is adapted based on available data throughout the year. If all sensors fail during a period, surface height after the gap is manually set based on the trend observed in valid data. These interpolated values should not be considered direct observations, though the overall trend remains reliable. All surface heights are referenced to the initial station installation (i.e., zero height at installation).

From the resulting z_surf_combined (see Fig. 12), z_ice_surf is recalculated as the one-year lagging minimum of z_surf_combined. This ensures that z_ice_surf reflects ablation during summer and remains stable during winter. Finally, snow_height is computed as the difference between z_surf_combined and z_ice_surf, representing the snow depth above the ice surface. These two variables are provided only for ablation area sites.

4.4 Thermistor Depth Estimation & 10m Ice/Firn Temperature Calculation

The thermistor strings measure temperature at depth at set intervals (e.g., every 1 m). At ablation sites the thermistor string slowly melts out and surfaces while at accumulation sites the thermistor string becomes buried. Thus, over time the initial depth at installation (noted in the raw data) is no longer the depth of measurement. This has been addressed in the following way: After we make our best estimation of the surface height, we can then specify the dates and depth of installation of thermistor strings to build a time-dependent depth variable for each thermistor. These depths are provided with the L3 data product and used to discard the recordings from surfaced thermistors which is common at the ablation stations. Once each temperature measurement has a depth tag, we can interpolate the firn/ice temperature at a standard 10 m depth. This standard depth has been used to be able to compare temporally and spatially various subsurface temperatures measurements (Vandecrux et al., 2024).

4.5 Data Examples

AWS data along two transects

To provide some insight into the data product, we show examples of data from AWSs along two transects: one crossing the ice sheet East-West starting at the KAN_L station and ending at TAS_A (Fig. 13) and the other going South – North starting at the QAS_U station and ending at the KPC_U station. The transects include data from both types of weather stations. The East-West transect shows the seasonal medians and standard deviation of weekly means of temperature and wind speed observations (Fig. 13) across the ice sheet. Above freezing seasonal medians are observed at the lower stations during summer on both sides of the ice sheet, while the coldest temperatures are observed in the interior ice sheet. This is also where the highest median and maximum weekly wind speeds are observed. The exception to this is TAS_A on the East coast located in a region

© Author(s) 2025. CC BY 4.0 License.



855

860



well-known for its piteraq storms (Van As et al., 2014b). This is reflected in the high maximum windspeeds found in summer and fall as well as high variability.

The South-North transect displays the major components of the surface energy balance (Fig. 14). Net shortwave radiation is the downward minus upward irradiance, which in principle, is always positive and highly dependent on the surface type. The sites in the ablation area will be on a bare ice surface with a much lower albedo than the sites in the accumulation area where the surface is snow covered. The net shortwave irradiance is furthermore affected by the total number of days where the sun is above the horizon, visualized by counting all the days with downward shortwave radiation higher than $1 \, \mathrm{W \, m^{-2}}$ (Fig. 14). The net longwave irradiance is on average negative, which means that the ice sheet is emitting more longwave radiation than it receives from the atmosphere and this means a cooling of the snow/ice. The latent turbulent heat flux is an energy exchange due to the phase changes of water at the ice sheet surface. The mean value is negative at most sites, meaning that evaporation or sublimation is removing energy from the surface. At NAU latent turbulent heat is however positive which means that the moisture in the air is condensing on the ice sheet and thereby imparting heat to the surface. Finally, the total energy from sensible turbulent heat flux is positive at all sites except for CP1. The sensible turbulent heat flux is the transfer of heat between the air and the ice sheet surface due to the temperature difference carried by moving air. When sensible heat flux is negative the ice sheet releases heat to the air.

5 Living Data & Continuous Improvements

The PROMICE | GC-NET programmes will continue to update and distribute data products as AWS data becomes available.

There may be undiscovered issues in the current dataset, and new challenges could emerge in future data collections.

5.1 Living data and FAIR principles

The PROMICE | GC-NET AWS data are managed in accordance with the FAIR principles (Wilkinson et al., 2016). All datasets are permanently archived in recognized open repositories and assigned persistent identifiers (DOIs). Each dataset is accompanied by rich, machine-readable metadata conforming to CF conventions where applicable (Eaton et al., 2024), including station identifiers, geographic coordinates, instrumentation details, sampling intervals, measurement units, and version history. Data are distributed in community-standard formats such as NetCDF (Rew and Davis, 1990; Unidata, 2023) with CF metadata and CSV with machine-readable headers, and they use controlled vocabularies and standardized units such as CF standard names to ensure interoperability. Access is open under the CC-BY 4.0 license. Provenance and processing history, including quality-control flags and software version information, are fully documented. Users are requested to cite the dataset using the assigned DOI and recommended citation format. When updates occur, dataset versions are tracked, and previous versions remain publicly accessible and discoverable at https://doi.org/10.22008/FK2/IW73UU (How et al., 2022a).

© Author(s) 2025. CC BY 4.0 License.





5.2 Known issues and continuous improvements

We have identified dataset problems that fall into three categories: tricky-to-spot issues, systematic errors that can be corrected in the data product, and errors caused by external factors such as people, animals, or equipment. The list below organizes the data issues we have observed according to these groups.

Tricky-to-spot issues:

- High variability in inclinometer readings, likely due to AWS shaking or instrument failure.
- Riming affecting multiple measured variables.
- Undocumented drift in AWS orientation.
 - Sonic ranger membrane lacking durability to consistently last between maintenance visits (instrument failure).
 - Instruments getting buried in snow during winter and/or spring.
 - Tripod collapse caused by compacting snow.
 - AWS toppling over due to extreme winds or unstable, crevassed terrain.
- Bent sensor boom from compacting snow, affecting the alignment of the radiometer and inclinometer.
 - Leaks, overfilling or artifical presurization of the pressure transducer assembly.
 - Electrostatic discharge from snow drift or damage to the AWS electrical circuit.
 - Delayed snow melt errors for the pluviometer. Snow accumulates in the gauge and is only registered as precipitation as
 it melts into the tipping bucket.

895 Systematic errors:

Identified dataset issues that we plan to correct for or implement in future data products:

- 1. Shading by instruments and station frame impacting albedo.
- 2. AWS orientation, which would influence the correction of the shortwave radiation and wind direction.
- 3. Data quality/certainty flags and error estimations.
- While we do our best to clean the data appropriately and address known issues (see above), we recognize that correcting issues is more complicated than simply documenting them, and that some corrections may not be possible, or may be subjective and a function of different use cases.

Errors caused by humans and animals:

© Author(s) 2025. CC BY 4.0 License.



Earth System Discussions

Science Data

- Human errors, such as swapping sensor plugs during maintenance or incorrect sensor mounting (e.g., wrong height or

orientation).

- Animal interference, including soiling of instruments or disturbance around the AWS site.

- Instrument malfunctions or hardware failures.

Additional sources of degradation include snow settling, freeze-thaw cycles, and ultraviolet radiation, which can affect mate-

rials such as carbon stakes.

910

915

930

935

To support transparency and collaboration, we maintain a user-contributable web-based database of known data quality is-

sues at: https://github.com/GEUS-Glaciology-and-Climate/PROMICE-AWS-data-issues (last accessed: 7 April 2025). This

system uses GitHub "issues" to log problems and challenges, with each entry tagged by relevant station, sensor, and year.

Users are encouraged to check the database for known issues related to their specific use of the dataset. If a new issue is identi-

fied, users can report it directly in the database. A PROMICE | GC-NET team member will review and verify the issue, mark it

as confirmed, and suggest a correction if appropriate. Verified issues will be addressed in future data releases. All issues remain

accessible, even after they are closed.

6 Summary

The updated PROMICE | GC-NET automatic weather station (AWS) data product provides a comprehensive overview of the

AWS network that monitors the Greenland Ice Sheet. This release focuses on key advancements in station design, instrumen-

tation, and the data processing workflow that together improve the quality, reliability, and scientific value of the observations.

Two primary AWS station designs are used across the network: the accumulation area mast stations and the ablation area

tripod stations. Accumulation area stations are constructed with a two-boom mast drilled into the firn and are optimized for

long-term stability in high-accumulation regions. These stations measure atmospheric parameters at two vertical levels, which

is essential for calculating turbulent fluxes. The ablation area stations, on the other hand, are designed around a one-boom free-

standing tripod system that is lightweight and ideal for deployment in the low-elevation ablation zones where surface melting

dominates. The tripod system rests on the ice surface and includes features like a suspended battery box to improve stability.

Substantial updates have been made to the instrumentation of both station types. Air temperature and humidity measurements

now rely on high-precision sensors such as the Vaisala HMP155E and OTT Lufft WS401, which are housed in fan-aspirated

radiation shields to reduce solar heating errors. Radiative fluxes are measured using Kipp & Zonen CNR4 radiometers, replac-

ing older models and enabling higher accuracy through better thermal stability and integrated tilt correction. Measurements of

snow accumulation and ice ablation are made using paired sonic rangers and pressure transducer assemblies. These are further

enhanced by structural changes to reduce issues like melt-out of stakes. Subsurface temperature profiles are obtained using

https://doi.org/10.5194/essd-2025-687

Preprint. Discussion started: 28 November 2025

© Author(s) 2025. CC BY 4.0 License.



945

Science Science Data

analog and digital thermistor strings, with depths extending to ten meters. AWSs are powered by a combination of solar panels and battery systems (both lead-acid and NiMH), and data transmission is handled via the Iridium Short Burst Data system to ensure global coverage even in remote polar regions. Data loggers have been upgraded to the CR1000X model, offering

940 improved speed, memory, and analog accuracy over the CR1000 logger.

Central to this release is the adoption of a robust, open-source data processing framework called pypromice. This Python-based workflow processes raw and transmitted data through several levels. Level 0 consists of raw measurements retrieved directly from the data loggers or received via satellite transmission. Level 1 converts these readings into physical units using calibration coefficients. Level 2 applies automated and manual filtering routines to remove outliers, correct persistent values, and flag suspect data based on known maintenance activities. Level 3 provides the final, user-ready dataset with both measured

and derived variables, including specific humidity, surface temperature, turbulent energy fluxes, cloud cover, and albedo.

The workflow accommodates both station formats and merges records from station upgrades or replacements to form longterm continuous datasets at each geographic site. This ensures data continuity and supports analyses over decadal timescales. Following the FAIR principles, the data products are available in both CSV and CF-compliant NetCDF formats, catering to a wide range of users. Public participation in data quality assurance is encouraged through an open GitHub repository, allowing

researchers to flag issues or suggest corrections, which are reviewed and incorporated by the PROMICE | GC-NET data team.

In summary, the PROMICE | GC-NET AWS data product update represents a significant advancement in Arctic climate monitoring. Through enhanced station designs, state-of-the-art instrumentation, and a transparent, automated data processing workflow, the dataset offers an essential resource for studying the Greenland Ice Sheet and its periphery, validating climate

models, and supporting global assessments of cryospheric change.

7 Code availability

The pypromice production pipeline is available for use and contributions at https://github.com/GEUS-Glaciology-and-Climate/pypromice, with a citeable DOI How et al. (2023a) (https://doi.org/10.22008/FK2/3TSBF0) alongside its corresponding, peer-

reviewed software publication How et al. (2023b).

8 Data availability

965

The PROMICE | GC-NET AWS dataset is primarily available through the GEUS Dataverse (https://doi.org/10.22008/FK2/IW73UU), which is updated monthly (How et al., 2022a). This version of the dataset has undergone both automatic and man-

ual quality control protocols.





Near-real-time PROMICE | GC-NET AWS data can be accessed from the GEUS Thredds server (https://thredds.geus.dk), which serves as an OPeNDAP access point for our operational datasets. The PROMICE | GC-NET AWS dataset is updated hourly with the latest transmission measurements from the station network. These measurements are collected, processed, and delivered to the GEUS Thredds server with a latency of approximately 10–15 minutes.

Author contributions. PH, ML, BV, DvA, KM, JB, and RF produced the AWS product through pypromice development. PH, BV and ML set up the data-curation framework. DvA, MC, AA, RF, CL, HJ, IS, BV, JB, and NK were in charge of the AWS designs and in field installations. Postprocessing routines were implemented by PH, ML, JB, and BV. In charge of the Example section: AS and SL. Appendix was compiled by IS and RF. AWS fieldwork and data assimilation: contributions from every co-authors. Responsible for AWS funding: SA, AA, SL, RF, MC, KL, AM, JA, RP, AB, JL, SB, and BH. Project management: SA, AA, SL, MC, and RF. RF prepared the manuscript with contributions from all co-authors.

Competing interests. Authors Kenneth D. Mankoff and Baptiste Vandecrux are part of the editorial board of ESSD.

Acknowledgements. AWS data from the Programme for Monitoring of the Greenland ice sheet (PROMICE), Greenland Climate Network (GC-NET), and the Greenland Ecological Monitoring Project (GEM) at the Geological Survey of Denmark and Greenland (GEUS) is available at How et al. (2022a). PROMICE and GC-Net is operated by The Department of Glaciology and Climate at the Geological Survey of Denmark and Greenland (GEUS) in collaboration with DTU Space and Asiaq Greenland survey. We thank past members of the PROMICE, GC-Net, and GlacioBasis teams for their contributions. KK acknowledge Greenland integrated observing system (GIOS). JA and RP acknowledge funding from the Austrian Science Fund (Grant DOI 10.55776/P35388 and 10.55776/P36306). SB was supported by a DSIT Greenland-UK Bursary Scheme. KM is supported by the NASA Modeling Analysis and Prediction program.





References

- Abermann, J., Van As, D., Wacker, S., Langley, K., Machguth, H., and Fausto, R. S.: Strong contrast in mass and energy balance between a coastal mountain glacier and the Greenland ice sheet, Journal of Glaciology, 65, 263–269, https://doi.org/10.1017/jog.2019.4, 2019.
- Abermann, J., Vandecrux, B., Scher, S., Löffler, K., Schalamon, F., Trügler, A., Fausto, R. S., and Schöner, W.: Learning from Al-990 fred Wegener's pioneering field observations in West Greenland after a century of climate change, Scientific Reports, 13, 8174, https://doi.org/10.1038/s41598-023-35192-7, 2023.
 - Ahlstrøm, A. P., Gravesen, P., Andersen, S. B., van As, D., Citterio, M., Fausto, R. S., Nielsen, S., Jepsen, H. F., Kristensen, S. S., Christensen, E. L., Stenseng, L., Forsberg, R., Hanson, S., Petersen, D., and project team, P.: A new programme for monitoring the mass loss of the Greenland ice sheet, GEUS Bulletin, 15, 61–64, https://doi.org/10.34194/geusb.v15.5045, part of Review of Survey Activities 2007, 2008.
- Aoki, T., Matoba, S., Uetake, J., Takeuchi, N., and Motoyama, H.: Field activities of the "Snow Impurity and Glacial Microbe effects on abrupt warming in the Arctic" (SIGMA) Project in Greenland in 2011-2013, Bulletin of Glaciological Research, 32, 3–20, 2014.
 - Bøggild, C. E., Olesen, O. B., Andreas, P. A., and Jørgensen, P.: Automatic glacier ablation measurements using pressure transducers, Journal of Glaciology, 50, 303–304, 2004.
- Box, J. E. and Steffen, K.: Sublimation on the Greenland ice sheet from automated weather station observations, Journal of Geophysical Research: Atmospheres, 106, 33 965–33 981, 2001.
 - Box, J. E., Hubbard, A., Bahr, D. B., Colgan, W. T., Fettweis, X., Mankoff, K. D., Wehrlé, A., Noël, B., van den Broeke, M. R., Wouters, B., Bjørk, A. A., and Fausto, R. S.: Greenland ice sheet climate disequilibrium and committed sea-level rise, Nature Climate Change, 12, 808–813, https://doi.org/10.1038/s41558-022-01441-2, 2022.
- Box, J. E., Nielsen, K. P., Yang, X., Niwano, M., Wehrlé, A., van As, D., Fettweis, X., Køltzow, M. A. o., Palmason, B., Fausto, R. S., van den
 Broeke, M. R., Huai, B., Ahlstrøm, A. P., Langley, K., Dachauer, A., and Noël, B.: Greenland ice sheet rainfall climatology, extremes and atmospheric river rapids, Meteorological Applications, 30, e2134, https://doi.org/https://doi.org/10.1002/met.2134, 2023.
 - Braithwaite, R. J. and Olesen, O. B.: Calculation of glacier ablation from air temperature, West Greenland, in: Glacier fluctuations and climatic change, pp. 219–233, Springer, 1989.
- Brock, B. W., Willis, I. C., and Sharp, M. J.: Measurement and parameterization of aerodynamic roughness length variations at Haut Glacier d'Arolla, Switzerland, Journal of Glaciology, 52, 281–297, 2006.
 - Chen, Z., Zheng, L., Zhang, B., Zhao, T., Zinglersen, K. B., Ding, M., Zhang, W., Hui, F., and Cheng, X.: The first Chinese automatic weather station on the Greenland ice sheet, Science Bulletin, 68, 452–455, https://doi.org/10.1016/j.scib.2023.02.012, 2023.
 - Citterio, M., van As, D., Ahlstrøm, A. P., Andersen, M. L., Andersen, S. B., Box, J. E., Charalampidis, C., Colgan, W. T., Fausto, R. S., Nielsen, S., et al.: Automatic weather stations for basic and applied glaciological research, Geological Survey of Denmark and Greenland Bulletin, pp. 69–72, 2015.
 - Claesson Liljedahl, L., Kontula, A., Harper, J., Näslund, J.-O., Selroos, J.-O., Pitkänen, P., Puigdomenech, I., Hobbs, M., Follin, S., Hirschorn, S., et al.: The Greenland Analogue Project: Final report, https://skb.com/publication/2484498/TR-14-13.pdf, 2016.
 - Cornillon, P., Gallagher, J., and Sgouros, T.: OPeNDAP: Accessing Data in a Distributed, Heterogeneous Environment, Data Science Journal, 2, 164–174, https://doi.org/10.2481/dsj.2.164, 2003.
- 1020 Eaton, B., Gregory, J., Drach, B., Taylor, K. E., Hankin, S., et al.: NetCDF Climate and Forecast (CF) Metadata Conventions, https://cfconventions.org/, version 1.x. Available at https://cfconventions.org/, 2024.





- Fausto, R. S., Van As, D., Ahlstrøm, A. P., and Citterio, M.: Assessing the accuracy of Greenland ice sheet ice ablation measurements by pressure transducer, Journal of Glaciology, 58, 1144–1150, 2012.
- Fausto, R. S., van As, D., Box, J. E., Colgan, W., and Langen, P. L.: Quantifying the surface energy fluxes in south Greenland during the 2012 high melt episodes using in-situ observations, Frontiers in Earth Science, 4, 82, 2016a.
 - Fausto, R. S., van As, D., Box, J. E., Colgan, W., Langen, P. L., and Mottram, R. H.: The implication of nonradiative energy fluxes dominating Greenland ice sheet exceptional ablation area surface melt in 2012, Geophysical Research Letters, 43, 2649–2658, 2016b.
 - Fausto, R. S., Abermann, J., and Ahlstrøm, A. P.: Annual Surface Mass Balance Records (2009–2019) From an Automatic Weather Station on Mittivakkat Glacier, SE Greenland, Frontiers in Earth Science, 8, https://doi.org/10.3389/feart.2020.00251, 2020.
- Fausto, R. S., van As, D., Mankoff, K. D., Vandecrux, B., Citterio, M., Ahlstrøm, A. P., Andersen, S. B., Colgan, W., Karlsson, N. B., Kjeldsen, K. K., Korsgaard, N. J., Larsen, S. H., Nielsen, S., ø. Pedersen, A., Shields, C. L., Solgaard, A. M., and Box, J. E.: Programme for Monitoring of the Greenland Ice Sheet (PROMICE) automatic weather station data, Earth System Science Data, 13, 3819–3845, https://doi.org/10.5194/essd-13-3819-2021, 2021.
- Fettweis, X., Box, J. E., Agosta, C., Amory, C., Kittel, C., Lang, C., van As, D., Machguth, H., and Gallée, H.: Reconstructions of the 1900–2015 Greenland ice sheet surface mass balance using the regional climate MAR model, The Cryosphere, 11, 1015–1033, https://doi.org/10.5194/tc-11-1015-2017, 2017.
 - Fettweis, X., Hofer, S., Krebs-Kanzow, U., Amory, C., Aoki, T., Berends, C. J., Born, A., Box, J. E., Delhasse, A., Fujita, K., Gierz, P., Goelzer, H., Hanna, E., Hashimoto, A., Huybrechts, P., Kapsch, M.-L., King, M. D., Kittel, C., Lang, C., Langen, P. L., Lenaerts, J. T. M., Liston, G. E., Lohmann, G., Mernild, S. H., Mikolajewicz, U., Modali, K., Mottram, R. H., Niwano, M., Noël, B., Ryan, J. C., Smith, A.,
- Streffing, J., Tedesco, M., van de Berg, W. J., van den Broeke, M., van de Wal, R. S. W., van Kampenhout, L., Wilton, D., Wouters, B., Ziemen, F., and Zolles, T.: GrSMBMIP: Intercomparison of the modelled 1980–2012 surface mass balance over the Greenland Ice Sheet, The Cryosphere, 14, 3935–3958, https://doi.org/10.5194/tc-14-3935-2020, 2020.
 - Goff, J. A. and Gratch, S.: Low-pressure properties of water-from 160 to 212° F., Trans. Am. Heat. Vent. Eng., 52, 95-121, 1946.
- Hanna, E., Pattyn, F., Navarro, F., Favier, V., Goelzer, H., van den Broeke, M. R., Vizcaino, M., Whitehouse, P. L., Ritz, C., Bulthuis, K.,
 and Smith, B.: Mass balance of the ice sheets and glaciers Progress since AR5 and challenges, Earth-Science Reviews, 201, 102 976, https://doi.org/10.1016/j.earscirev.2019.102976, 2020.
 - Harrison, R. G., Chalmers, N., and Hogan, R. J.: Retrospective cloud determinations from surface solar radiation measurements, Atmospheric Research, 90, 54–62, 2008.
- Hassell, D., Gregory, J., Blower, J., Lawrence, B. N., and Taylor, K. E.: A data model of the Climate and Forecast metadata conventions (CF1.6) with a software implementation (cf-python v2.1), Geoscientific Model Development, 10, 4619–4646, https://doi.org/10.5194/gmd10-4619-2017, 2017.
 - Holtslag, A. and De Bruin, H.: Applied modeling of the nighttime surface energy balance over land, Journal of Applied Meteorology and Climatology, 27, 689–704, 1988.
- How, P., Lund, M., Ahlstrøm, A., Andersen, S., Box, J., Citterio, M., Colgan, W., Fausto, R., Karlsson, N., Jakobsen, J., Jakobsen, J., Jakobsen, J., Larsen, S., Mankoff, K., Nielsen, R., Rutishauser, A., Shield, C., Solgaard, A., Stevens, I., van As, D., Vandecrux, B., Abermann, J., Bjørk, A., Langley, K., Lea, J., and Prinz, R.: PROMICE and GC-Net automated weather station data in Greenland, https://doi.org/10.22008/FK2/IW73UU, 2022a.



1060



- How, P., Lund, M., Ahlstrøm, A., Andersen, S., Box, J., Citterio, M., Colgan, W., Fausto, R., Karlsson, N., Jakobsen, J., Jakobsegaard, H., Larsen, S., Mankoff, K., Nielsen, R., Rutishauser, A., Shield, C., Solgaard, A., Stevens, I., van As, D., Vandecrux, B., Abermann, J., Bjørk, A., Langley, K., Lea, J., and Prinz, R.: AWS data_readme.pdf, https://doi.org/10.22008/FK2/IW73UU/XCAQHJ, 2022b.
- How, P., Lund, M., Nielsen, R., Ahlstrøm, A., Fausto, R., Larsen, S., Mankoff, K., Vandecrux, B., and Wright, P.: pypromice v1.5.3, https://doi.org/10.22008/FK2/3TSBF0, 2023a.
- How, P., Wright, P. J., Mankoff, K. D., Vandecrux, B., Fausto, R. S., and Ahlstrøm, A. P.: pypromice: A Python package for processing automated weather station data, Journal of Open Source Software, 8, 5298, https://doi.org/10.21105/joss.05298, 2023b.
- Hynek, B., Binder, D., Citterio, M., Larsen, S. H., Abermann, J., Verhoeven, G., Ludewig, E., and Schöner, W.: Accumulation by avalanches as a significant contributor to the mass balance of a peripheral glacier of Greenland, The Cryosphere, 18, 5481–5494, https://doi.org/10.5194/tc-18-5481-2024, 2024.
 - Khan, S. A., Seroussi, H., Morlighem, M., Colgan, W., Helm, V., Cheng, G., Berg, D., Barletta, V. R., Larsen, N. K., Kochtitzky, W., van den Broeke, M., Kjær, K. H., Aschwanden, A., Noël, B., Box, J. E., MacGregor, J. A., Fausto, R. S., Mankoff, K. D., Howat, I. M., Oniszk,
- 1070 K., Fahrner, D., Løkkegaard, A., Lippert, E. Y. H., Bråtner, A., and Hassan, J.: Smoothed monthly Greenland ice sheet elevation changes during 2003–2023, Earth System Science Data, 17, 3047–3071, https://doi.org/10.5194/essd-17-3047-2025, 2025.
 - Kokhanovsky, A., Box, J. E., Vandecrux, B., Mankoff, K. D., Lamare, M., Smirnov, A., and Kern, M.: The determination of snow albedo from satellite measurements using fast atmospheric correction technique, Remote Sensing, 12, 234, 2020.
- Larsen, S. H., Binder, D., Rutishauser, A., Hynek, B., Fausto, R. S., and Citterio, M.: Climate and ablation observations from automatic ablation and weather stations at A. P. Olsen Ice Cap transect, northeast Greenland, for May 2008 through May 2022, Earth System Science Data, 16, 4103–4118, https://doi.org/10.5194/essd-16-4103-2024, 2024.
 - Mankoff, K. D., Solgaard, A., Colgan, W., Ahlstrøm, A. P., Khan, S. A., and Fausto, R. S.: Greenland Ice Sheet solid ice discharge from 1986 through March 2020, Earth System Science Data, 12, 1367–1383, https://doi.org/10.5194/essd-12-1367-2020, 2020.
- Messerli, A., Arthur, J., Langley, K., How, P., and Abermann, J.: Snow cover evolution at Qasigiannguit Glacier, southwest Greenland, Frontiers in Earth Science, 10, https://doi.org/10.3389/feart.2022.970026, 2022.
 - Miller, N. B., Shupe, M. D., Cox, C. J., Noone, D., Persson, P. O. G., and Steffen, K.: Surface energy budget responses to radiative forcing at Summit, Greenland, The Cryosphere, 11, 497–516, 2017.
 - Mouginot, J., Rignot, E., van den Broeke, M. R., Millan, R., Morlighem, M., Noël, B., Scheuchl, B., and Wood, M.: Forty-six years of Greenland Ice Sheet mass balance from 1972 to 2018, Proceedings of the National Academy of Sciences, 116, 9239–9244, https://doi.org/10.1073/pnas.1904242116, 2019.
 - Nativi, S., Manzella, G. M. R., Paolucci, F., Mazzetti, P., Pecci, L., Bigagli, L., and Reseghetti, F.: Federated data bases for the development of an operational monitoring and forecasting system of the ocean: the THREDDS Dataset Merger, Advances in Geosciences, 8, 39–47, https://doi.org/10.5194/adgeo-8-39-2006, 2006.
- Noël, B., Berg, W. J. v. d., Wessem, J., Meijgaard, E. v., As, D. v., Lenaerts, J., Lhermitte, S., Kuipers Munneke, P., Smeets, C., Ulft, L.

 H. v., et al.: Modelling the climate and surface mass balance of polar ice sheets using RACMO2–Part 1: Greenland (1958–2016), The Cryosphere, 12, 811–831, 2018.
 - OPeNDAP, Inc.: OPeNDAP: The Open-source Project for a Network Data Access Protocol, https://www.opendap.org/, comprehensive User Guide. Available at https://opendap.github.io/documentation/UserGuideComprehensive.pdf, 2024.
- Otosaka, I. N., Shepherd, A., Ivins, E. R., Schlegel, N.-J., Amory, C., van den Broeke, M. R., Horwath, M., Joughin, I., King, M. D., Krinner, G., Nowicki, S., Payne, A. J., Rignot, E., Scambos, T., Simon, K. M., Smith, B. E., Sørensen, L. S., Velicogna, I., Whitehouse, P. L., A,





- G., Agosta, C., Ahlstrøm, A. P., Blazquez, A., Colgan, W., Engdahl, M. E., Fettweis, X., Forsberg, R., Gallée, H., Gardner, A., Gilbert, L., Gourmelen, N., Groh, A., Gunter, B. C., Harig, C., Helm, V., Khan, S. A., Kittel, C., Konrad, H., Langen, P. L., Lecavalier, B. S., Liang, C.-C., Loomis, B. D., McMillan, M., Melini, D., Mernild, S. H., Mottram, R., Mouginot, J., Nilsson, J., Noël, B., Pattle, M. E., Peltier, W. R., Pie, N., Roca, M., Sasgen, I., Save, H. V., Seo, K.-W., Scheuchl, B., Schrama, E. J. O., Schröder, L., Simonsen, S. B., Slater, T., Spada, G.,
- Sutterley, T. C., Vishwakarma, B. D., van Wessem, J. M., Wiese, D., van der Wal, W., and Wouters, B.: Mass balance of the Greenland and Antarctic ice sheets from 1992 to 2020, Earth System Science Data, 15, 1597–1616, https://doi.org/10.5194/essd-15-1597-2023, 2023.
 - Paulson, C. A.: The mathematical representation of wind speed and temperature profiles in the unstable atmospheric surface layer, Journal of Applied Meteorology and Climatology, 9, 857–861, 1970.
- Poinar, K., Box, J. E., Mote, T. L., Loomis, B. D., Smith, B. E., Medley, B. C., Askjaer, T. G., Mankoff, K. D., Fausto, R. S., and Tedesco, M.: Greenland Ice Sheet, Tech. rep., NOAA Arctic Report Card 2024, https://doi.org/10.25923/njxd-b826, 2024.
 - Poinar, K., Box, J. E., Mote, T. L., Fettweis, X., Loomis, B. D., Smith, B. E., Medley, B. C., Mankoff, K. D., Askjaer, T. G., Scheller, J. H., Fausto, R. S., and Tedesco, M.: Greenland Ice Sheet, in: State of the Climate in 2024, edited by Blunden, J. and Boyer, T., vol. 106, pp. S338–S341, https://doi.org/10.1175/BAMS-D-25-0104.1, 2025.
- Prinz, R., Abermann, J., and Steiner, J.: LATTICE Land-terminating ice cliffs in North Greenland: Processes, drivers and their relation to regional climate, Austrian Science Fund (FWF) Project P36306, https://doi.org/10.55776/P36306, funding period: 2023–2027, 2023.
 - Python Software Foundation: Python Language Reference, version 3.x, https://www.python.org/, available at https://docs.python.org/3/reference/, 2024.
 - Rew, R. and Davis, G.: NetCDF: an interface for scientific data access, IEEE Computer Graphics and Applications, 10, 76–82, https://api. semanticscholar.org/CorpusID:11171299, 1990.
- Ryan, J., Hubbard, A., Irvine-Fynn, T. D., Doyle, S. H., Cook, J., Stibal, M., and Box, J.: How robust are in situ observations for validating satellite-derived albedo over the dark zone of the Greenland Ice Sheet?, Geophysical Research Letters, 44, 6218–6225, 2017.
 - Schneebeli, M., Pielmeier, C., and Johnson, J. B.: Measuring snow microstructure and hardness using a high resolution penetrometer, Cold Regions Science and Technology, 30, 101–114, https://doi.org/https://doi.org/10.1016/S0165-232X(99)00030-0, 1999.
- Shepherd, A., Ivins, E., Rignot, E., Smith, B., van den Broeke, M., Velicogna, I., Whitehouse, P., Briggs, K., Joughin, I., Krinner, G., Nowicki, S., Payne, T., Scambos, T., Schlegel, N., Geruo, A., Agosta, C., Ahlstrøm, A., Babonis, G., Barletta, V. R., Bjørk, A. A., Blazquez, A.,
- Bonin, J., Colgan, W., Csatho, B., Cullather, R., Engdahl, M. E., Felikson, D., Fettweis, X., Forsberg, R., Hogg, A. E., Gallee, H., Gardner, A., Gilbert, L., Gourmelen, N., Groh, A., Gunter, B., Hanna, E., Harig, C., Helm, V., Horvath, A., Horwath, M., Khan, S., Kjeldsen, K. K., Konrad, H., Langen, P. L., Lecavalier, B., Loomis, B., Luthcke, S., McMillan, M., Melini, D., Mernild, S., Mohajerani, Y., Moore, P.,
- Mottram, R., Mouginot, J., Moyano, G., Muir, A., Nagler, T., Nield, G., Nilsson, J., Noël, B., Otosaka, I., Pattle, M. E., Peltier, W. R., Pie, N., Rietbroek, R., Rott, H., Sørensen, L. S., Sasgen, I., Save, H., Scheuchl, B., Schrama, E., Schröder, L., Seo, K.-W., Simonsen, S. B.,
- Slater, T., Spada, G., Sutterley, T., Talpe, M., Tarasov, L., van de Berg, W. J., van der Wal, W., van Wessem, M., Vishwakarma, B. D., Wiese, D., Wilton, D., Wagner, T., Wouters, B., and Wuite, J.: Mass balance of the Greenland Ice Sheet from 1992 to 2018, Nature, 579, 233–239, https://doi.org/10.1038/s41586-019-1855-2, 2020.
- Smeets, C. and Van den Broeke, M.: The parameterisation of scalar transfer over rough ice, Boundary-layer meteorology, 128, 339–355, 2008a.
 - Smeets, C. and Van den Broeke, M.: Temporal and spatial variations of the aerodynamic roughness length in the ablation zone of the Greenland ice sheet, Boundary-layer meteorology, 128, 315–338, 2008b.

https://doi.org/10.5194/essd-2025-687 Preprint. Discussion started: 28 November 2025 © Author(s) 2025. CC BY 4.0 License.



1135



- Smeets, P. C., Kuipers Munneke, P., Van As, D., van den Broeke, M. R., Boot, W., Oerlemans, H., Snellen, H., Reijmer, C. H., and van de Wal, R. S.: The K-transect in west Greenland: Automatic weather station data (1993–2016), Arctic, Antarctic, and Alpine Research, 50, \$100,002,2018.
- Solgaard, A., Kusk, A., Merryman Boncori, J. P., Dall, J., Mankoff, K. D., Ahlstrøm, A. P., Andersen, S. B., Citterio, M., Karlsson, N. B., Kjeldsen, K. K., Korsgaard, N. J., Larsen, S. H., and Fausto, R. S.: Greenland ice velocity maps from the PROMICE project, Earth System Science Data, 13, 3491–3512, https://doi.org/10.5194/essd-13-3491-2021, 2021.
- Steffen, K. and Box, J. E.: Surface climatology of the Greenland Ice Sheet: Greenland Climate Network 1995–1999, Journal of Geophysical Research: Atmospheres, 106, 33 951–33 964, https://doi.org/10.1029/2001JD900161, 2001.
 - Steffen, K., Box, J. E., and Abdalati, W.: Greenland Climate Network: GC-Net, Crrel monograph, U.S. Army Cold Regions Research and Engineering Laboratory (CRREL), tribute to M. Meier, 1996.
 - Stober, M., Hitziger, T., Näke, L., Heim, J., and Hepperle, J.: Dreißig Jahre Eishöhenänderungen am Swiss Camp (Grönland), Polarforschung, 91, 95–104, https://doi.org/10.5194/polf-91-95-2023, 2023.
- Studinger, M.: IceBridge ATM L2 Icessn Elevation, Slope, and Roughness, https://doi.org/10.5067/CPRXXK3F39RV, elevation variable: "z" data, 2014.
 - Swinbank, W. C.: Long-wave radiation from clear skies, Quarterly Journal of the Royal Meteorological Society, 89, 339-348, 1963.
 - Thomas, R. and Studinger, M.: Pre-IceBridge ATM L2 Icessn Elevation, Slope, and Roughness, Version 1, https://doi.org/10.5067/6C6WA3R918HJ, 2010.
- 1150 Unidata: NetCDF (Network Common Data Form): Data Model, Interface, and Library, https://www.unidata.ucar.edu/software/netcdf/, version 4.x. Available from the Unidata Program Center, Boulder, Colorado, USA., 2023.
 - Van As, D.: Warming, glacier melt and surface energy budget from weather station observations in the Melville Bay region of northwest Greenland, Journal of Glaciology, 57, 208–220, 2011.
- Van As, D., Van Den Broeke, M., Reijmer, C., and Van De Wal, R.: The summer surface energy balance of the high Antarctic plateau, 1155 Boundary-Layer Meteorology, 115, 289–317, 2005.
 - Van As, D., Fausto, R. S., and project team, P.: Programme for Monitoring of the Greenland Ice Sheet (PROMICE): first temperature and ablation records, Geological Survey of Denmark and Greenland (GEUS) Bulletin, 23, 73–76, 2011.
 - Van As, D., Fausto, R. S., Colgan, W. T., and Box, J. E.: Darkening of the Greenland ice sheet due to the meltalbedo feedback observed at PROMICE weather stations, Geological Survey of Denmark and Greenland (GEUS) Bulletin, 28, 69–72, 2013.
- Van As, D., Andersen, M. L., Petersen, D., Fettweis, X., Van Angelen, J. H., Lenaerts, J. T., Van Den Broeke, M. R., Lea, J. M., Bøggild, C. E., Ahlstrøm, A. P., et al.: Increasing meltwater discharge from the Nuuk region of the Greenland ice sheet and implications for mass balance (1960–2012), Journal of Glaciology, 60, 314–322, 2014a.
 - Van As, D., Fausto, R. S., Steffen, K., et al.: Katabatic winds and piteraq storms: Observations from the Greenland ice sheet, Geological Survey of Denmark and Greenland (GEUS) Bulletin, 31, 83–86, 2014b.
- van den Broeke, M., van As, D., Reijmer, C., and van de Wal, R.: Assessing and improving the quality of unattended radiation observations in Antarctica, Journal of Atmospheric and Oceanic Technology, 21, 1417–1431, 2004.
 - Vandecrux, B., Mottram, R., Langen, P. L., Fausto, R. S., Olesen, M., Stevens, C. M., Verjans, V., Leeson, A., Ligtenberg, S., Kuipers Munneke, P., et al.: The firn meltwater Retention Model Intercomparison Project (RetMIP): Evaluation of nine firn models at four weather station sites on the Greenland ice sheet, The Cryosphere, 14, 3785–3810, 2020.

https://doi.org/10.5194/essd-2025-687 Preprint. Discussion started: 28 November 2025 © Author(s) 2025. CC BY 4.0 License.





- 1170 Vandecrux, B., Box, J. E., Ahlstrøm, A. P., Andersen, S. B., Bayou, N., Colgan, W. T., Cullen, N. J., Fausto, R. S., Haas-Artho, D., Heilig, A., Houtz, D. A., How, P., Enescu, I. I., Karlsson, N. B., Buchholz, R. K., Mankoff, K. D., McGrath, D., Molotch, N. P., Perren, B., Revheim, M. K., Rutishauser, A., Sampson, K., Schneebeli, M., Starkweather, S., Steffen, S., Weber, J., Wright, P. J., Zwally, H. J., and Steffen, K.: The historical Greenland Climate Network (GC-Net) curated and augmented level-1 dataset, Earth System Science Data, 15, 5467–5493, https://doi.org/10.5194/essd-15-5467-2023, 2023.
- 1175 Vandecrux, B., Fausto, R. S., Box, J. E., Covi, F., Hock, R., Rennermalm, Å. K., Heilig, A., Abermann, J., van As, D., Bjerre, E., Fettweis, X., Smeets, P. C. J. P., Kuipers Munneke, P., van den Broeke, M. R., Brils, M., Langen, P. L., Mottram, R., and Ahlstrøm, A. P.: Recent warming trends of the Greenland ice sheet documented by historical firn and ice temperature observations and machine learning, The Cryosphere, 18, 609–631, https://doi.org/10.5194/tc-18-609-2024, 2024.
- Wilkinson, M. D., Dumontier, M., Aalbersberg, I. J., Appleton, G., Axton, M., Baak, A., Blomberg, N., Boiten, J., da Silva Santos, L. B.,
 Bourne, P. E., Bouwman, J., Brookes, A. J., Clark, T., Crosas, M., Dillo, I., Dumon, O., Edmunds, S., Evelo, C. T., Finkers, R., Gonzalez-Beltran, A., Gray, A. J. G., Groth, P., Goble, C., Grethe, J. S., Heringa, J., 't Hoen, P. A. C., Hooft, R., Kuhn, T., Kok, R., Kok, J., Lusher, S. J., Martone, M. E., Mons, B., Packer, A. L., Persson, B., Rocca-Serra, P., Roos, M., van Schaik, R., Sansone, S., Schultes, E., Sengstag, T., Slater, T., Strawn, G., Swertz, M. A., Thompson, M., van der Lei, J., van Mulligen, E., Velterop, J., Waagmeester, A., Wittenburg, P., Wolstencroft, K., Zhao, J., and Mons, B.: The FAIR Guiding Principles for scientific data management and stewardship, Scientific Data,
 3, 160 018, https://doi.org/10.1038/sdata.2016.18, 2016.
 - Yang, D., Ishida, S., Goodison, B. E., and Gunther, T.: Bias correction of daily precipitation measurements for Greenland, Journal of Geophysical Research: Atmospheres, 104, 6171–6181, https://doi.org/https://doi.org/10.1029/1998JD200110, 1999.





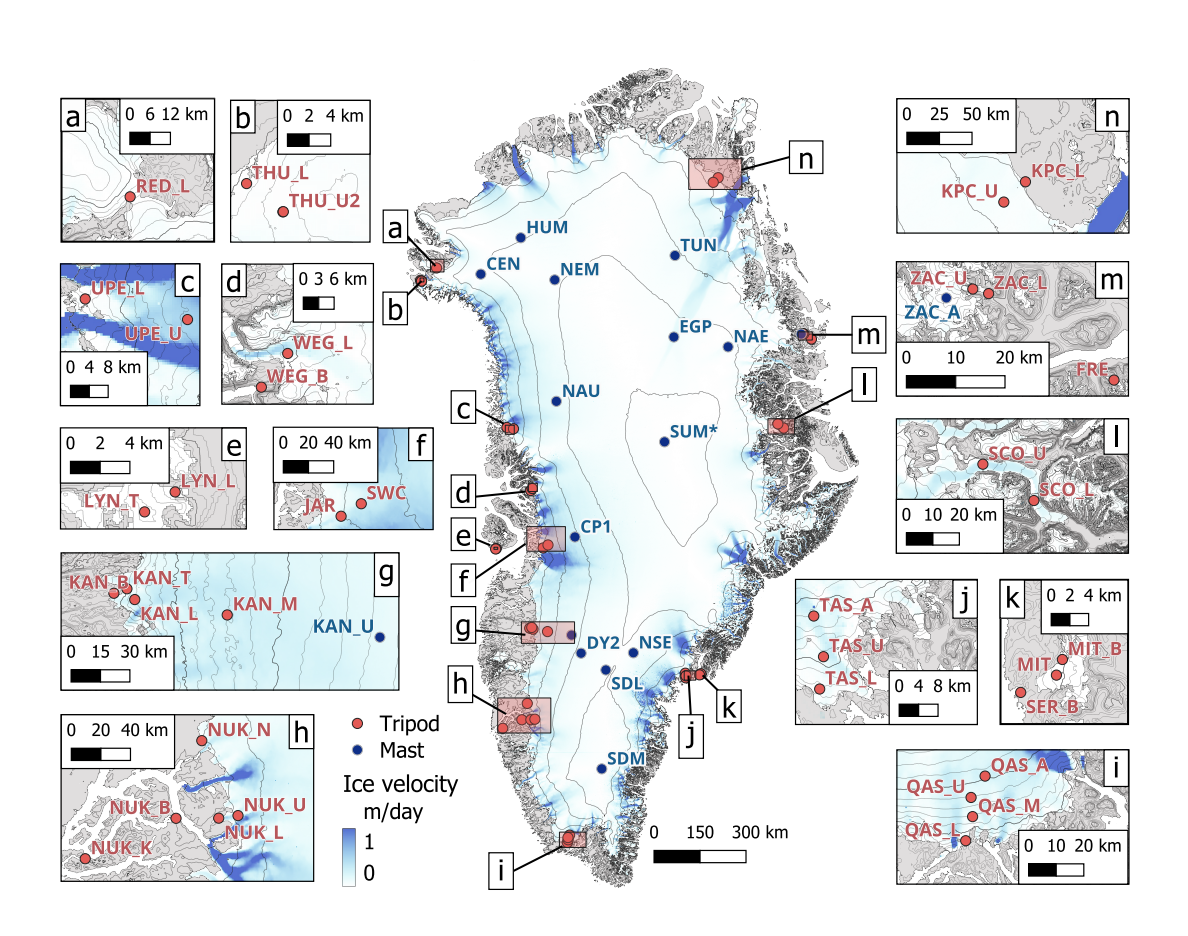


Figure 1. Map of Greenland with the latest GEUS and externally owned automatic weather station locations (Table 1).





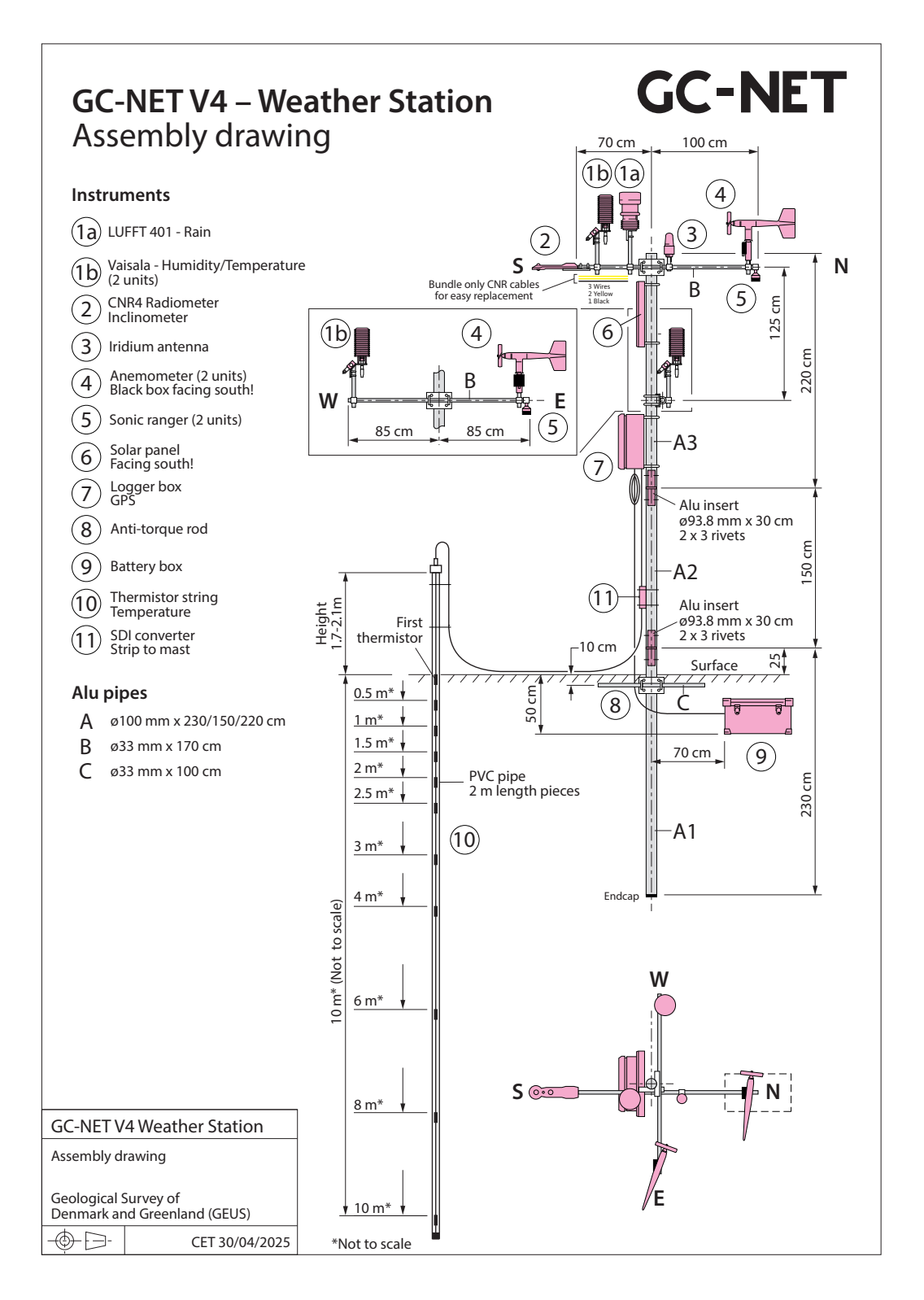


Figure 2. Schematic of an accumulation area design AWS.



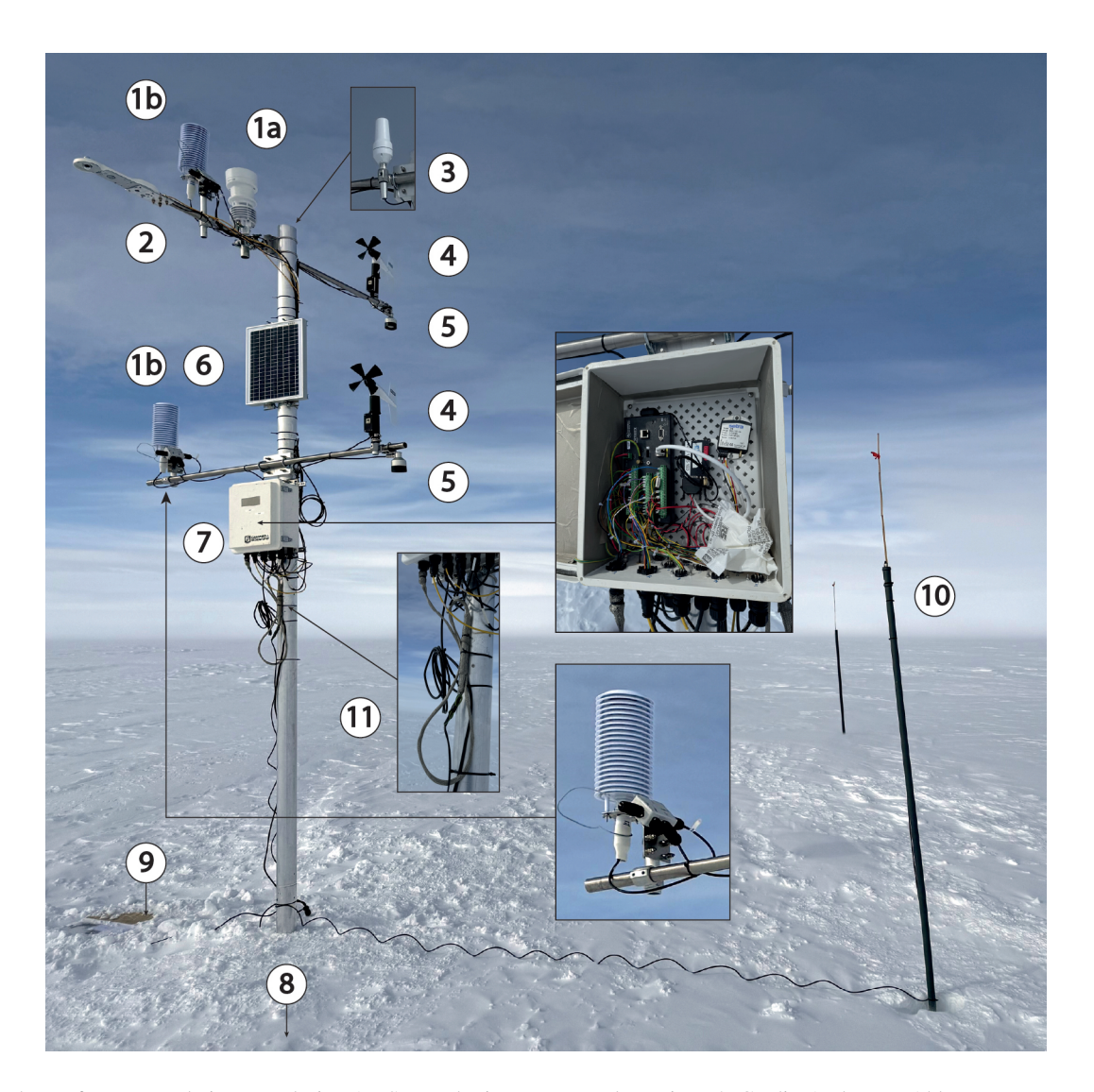


Figure 3. Photo of an accumulation area design AWS. Numbering corresponds to Figure 2. Credit: Andreas P. Ahlstrøm.





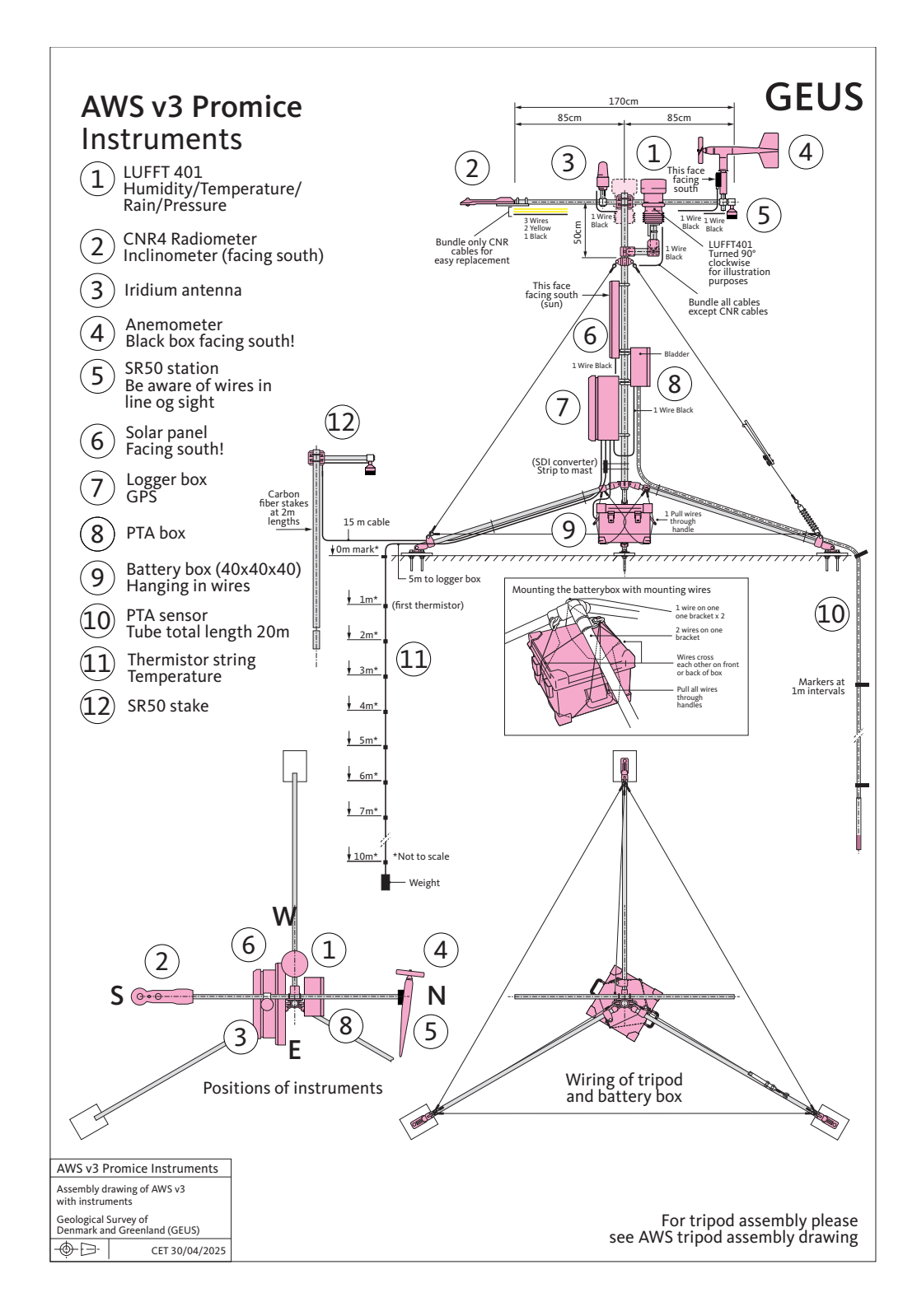


Figure 4. Schematic of an ablation area design AWS.



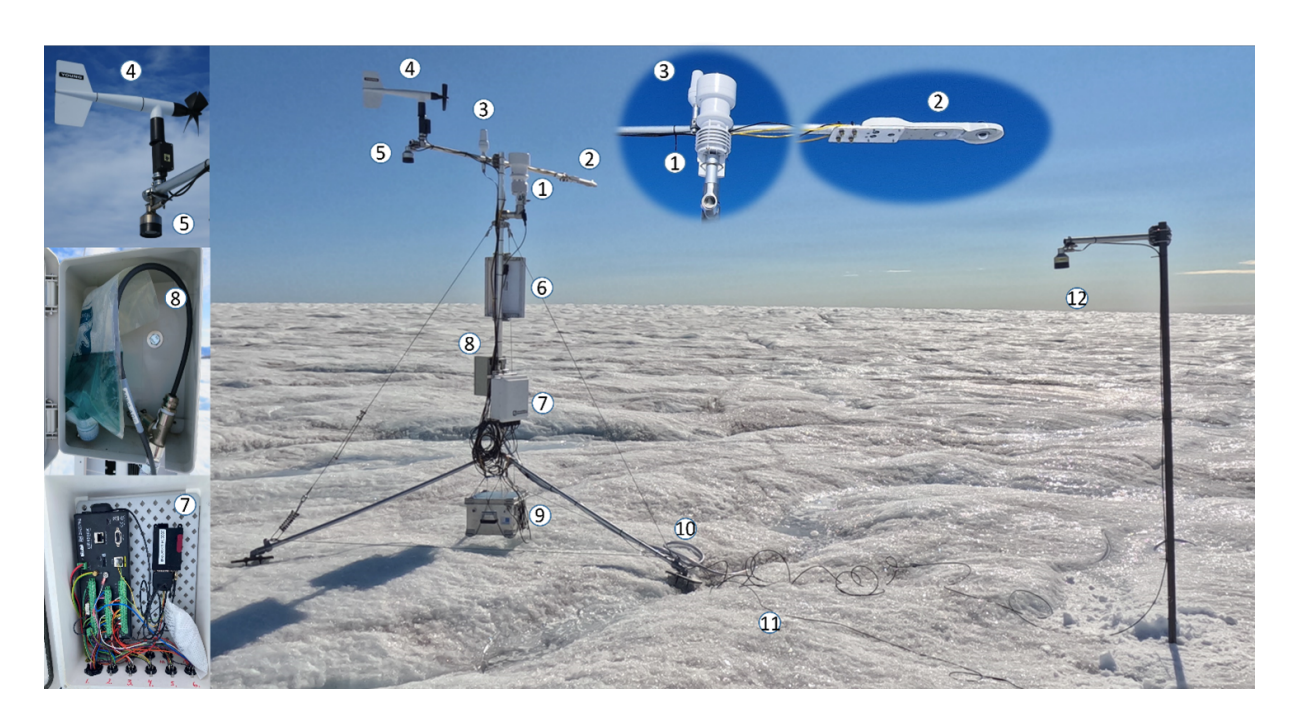


Figure 5. QAS_M ablation area AWS photographed 1. September 2024 on the Greenland ice sheet. Instrument numbering corresponds to Figure 4. Credit: Jason E. Box.





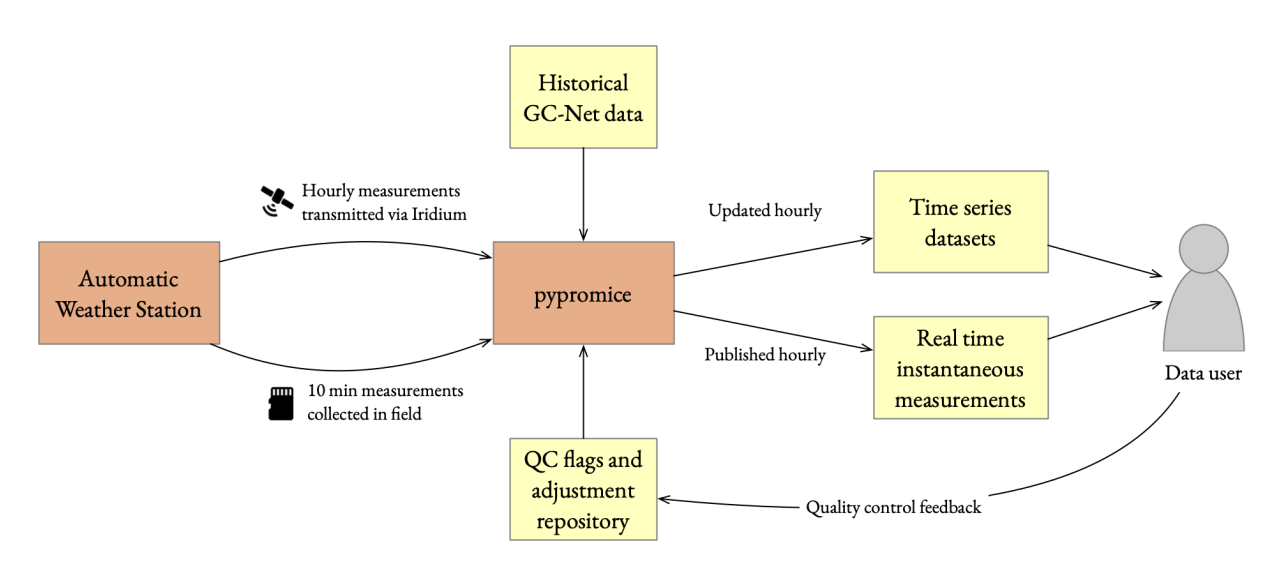


Figure 6. Operational components and key data inputs of the PROMICE pipeline, combining AWS measurements, historical GC-Net data, and QC adjustments in pypromice to produce hourly updated time series and real-time measurements.





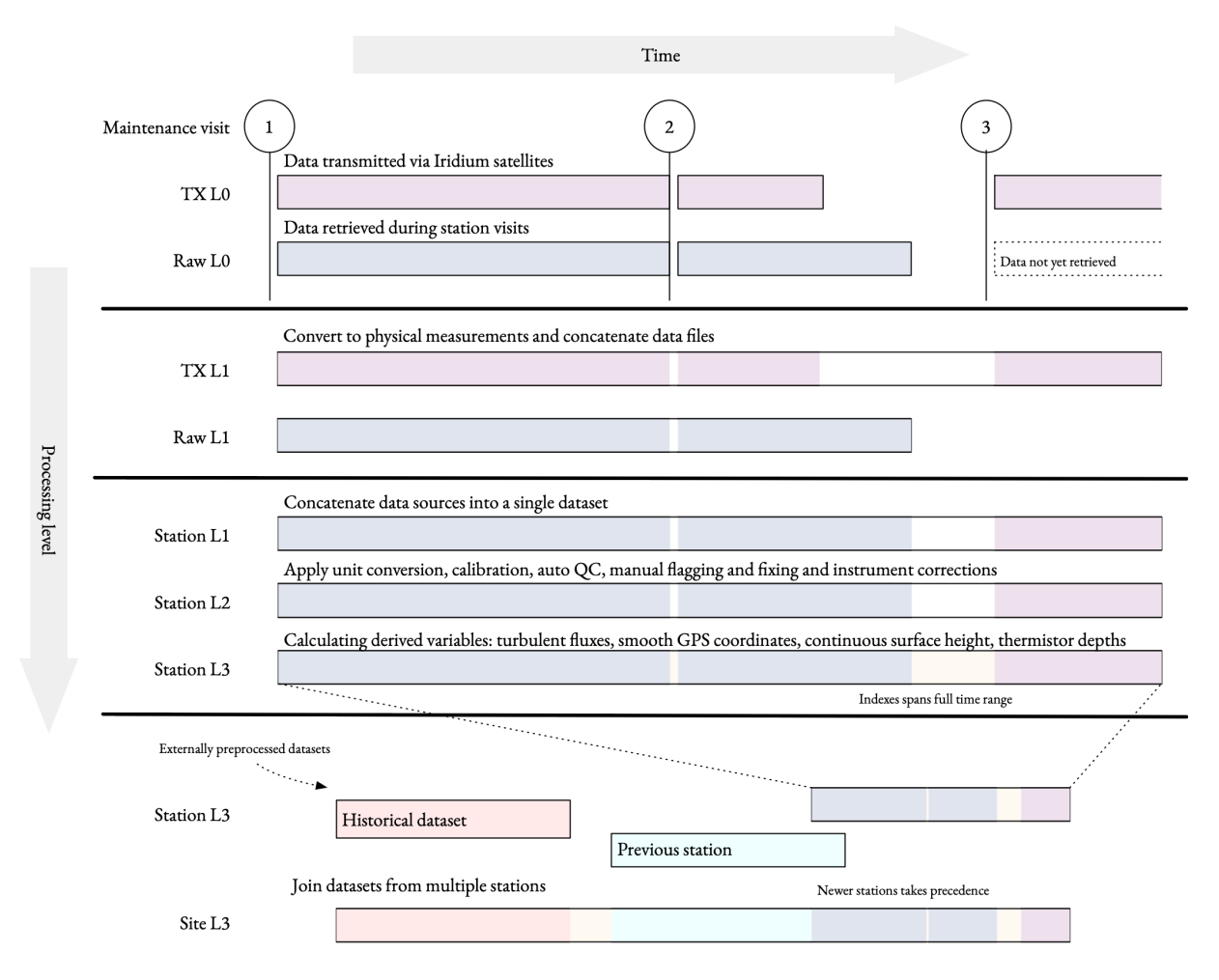


Figure 7. Illustration of the AWS data processing pipeline from raw L0 chunks to final L3 site-specific products. The horizontal axis shows measurement time; the vertical axis shows processing level. Station-specific L1–L3 series are generated from L0 data and merged with historical and previous-station datasets (bottom) to produce continuous site-level time series. Colors indicate data sources, white denotes gaps, and light yellow marks gap-spanning with indices and, in some cases, value filling.





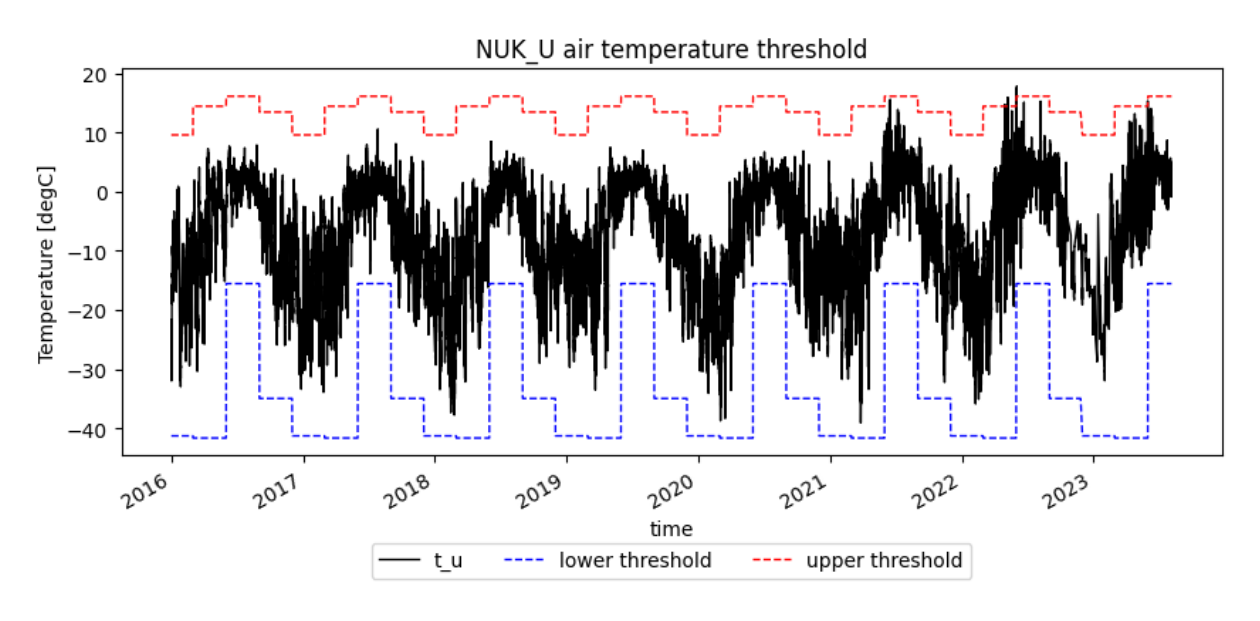


Figure 8. Example of how the percentile filter operates for air temperature.





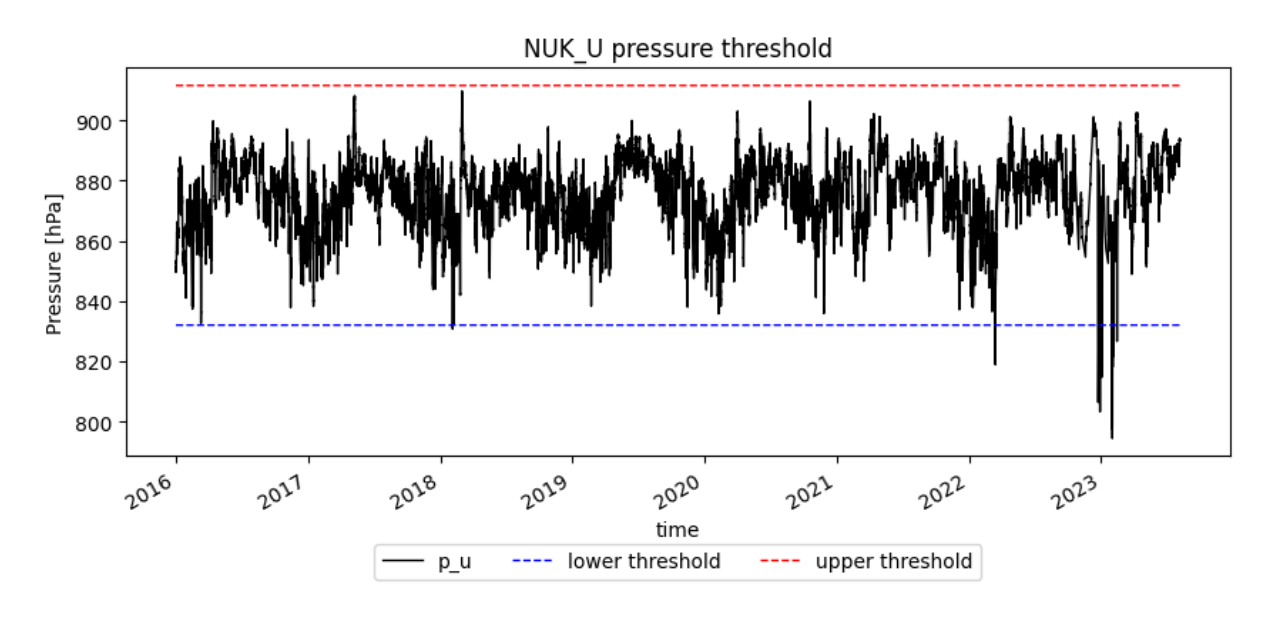


Figure 9. Example of how the percentile filter operates for air pressure.





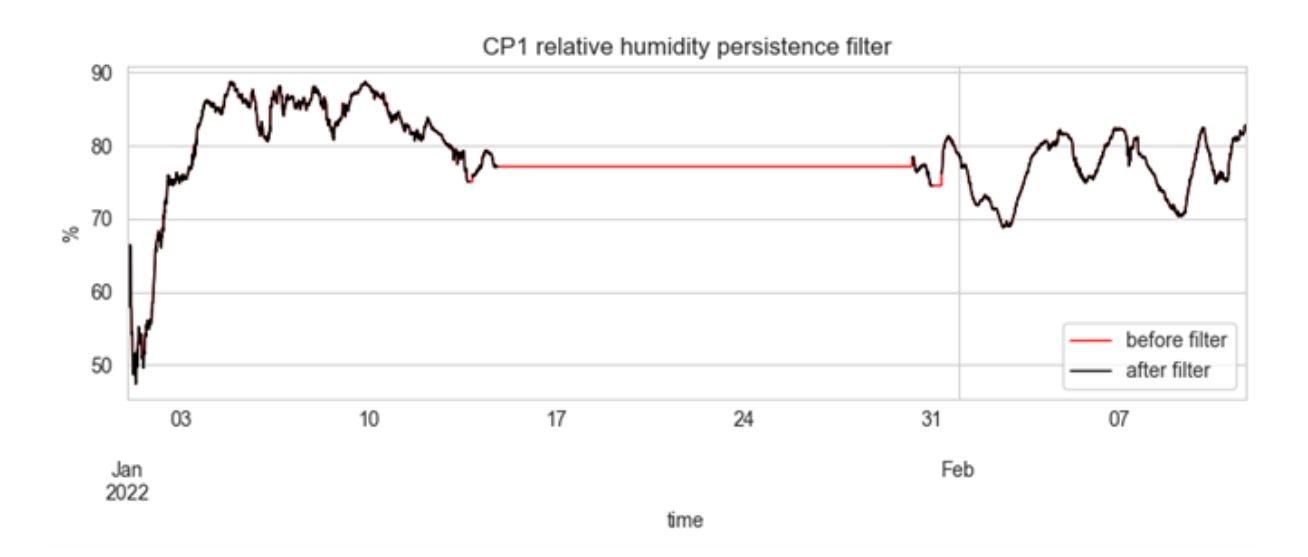


Figure 10. Illustration of how the persistence filter operates.



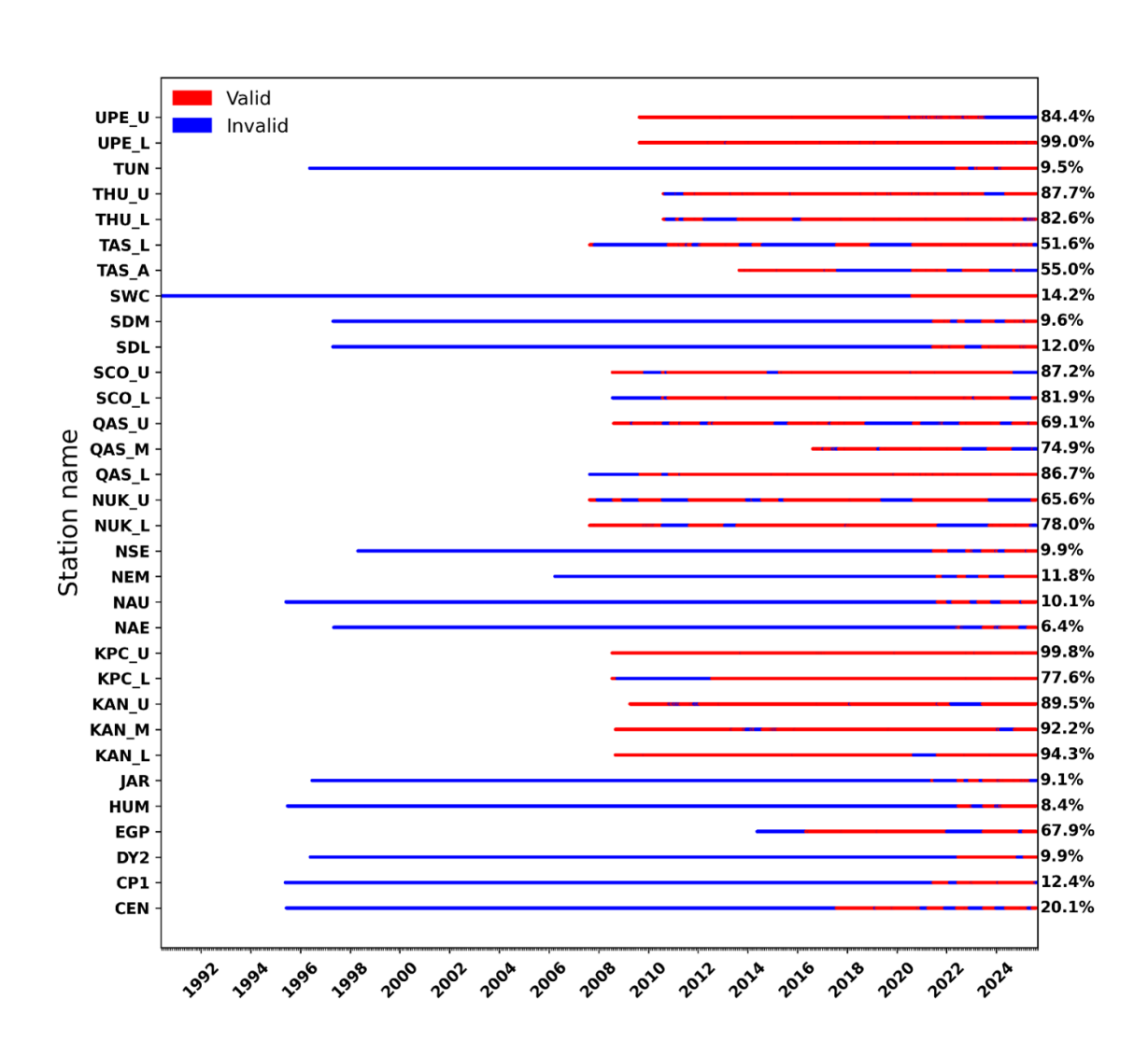


Figure 11. Combined availability of the eight key variables needed to calculate the surface energy balance (SEB) from daily data products (last data entry 2025-04-01).



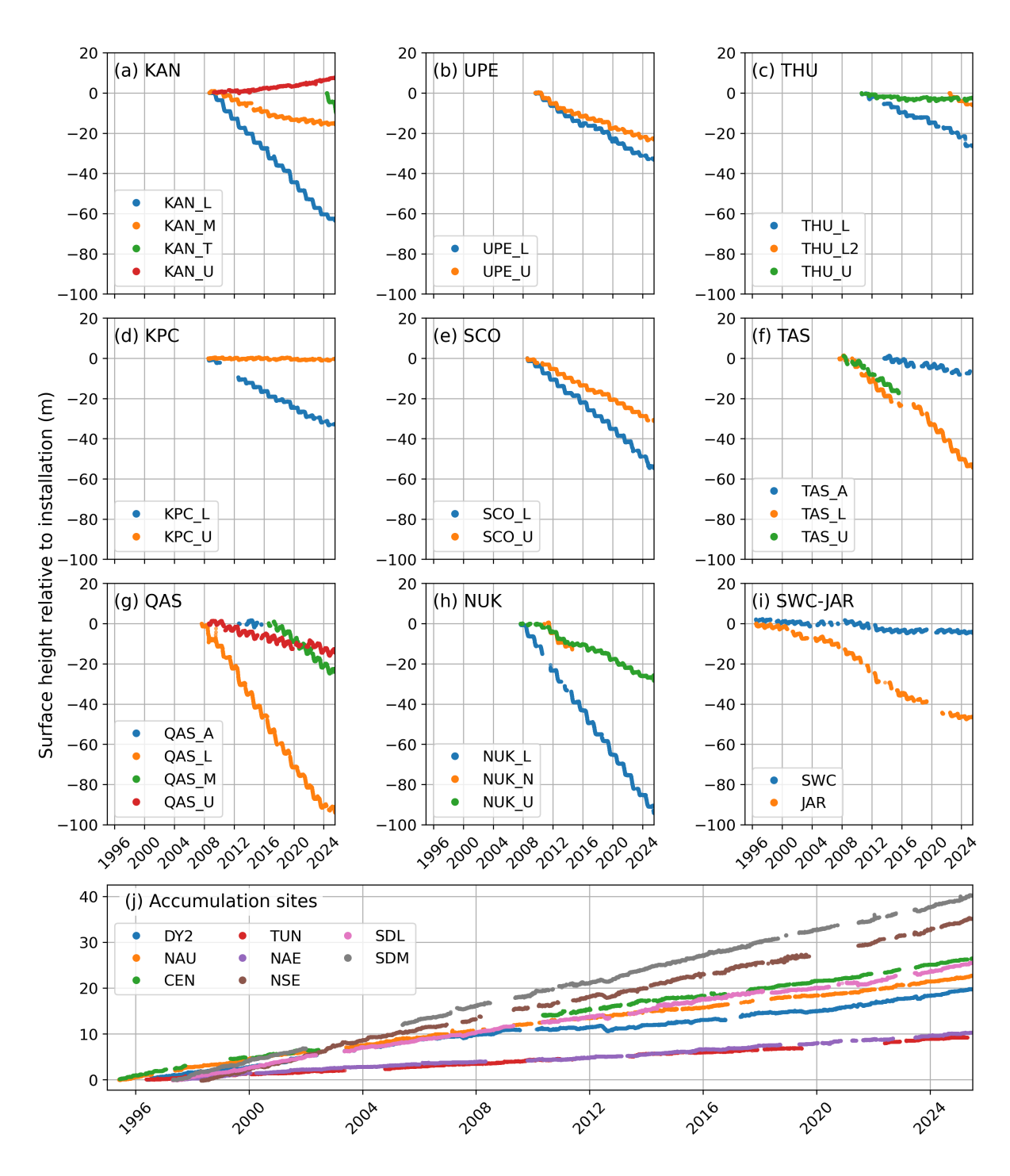


Figure 12. The variable <code>z_surf_combined</code> illustrated for all PROMICE | GC-NET ice sheet sites.





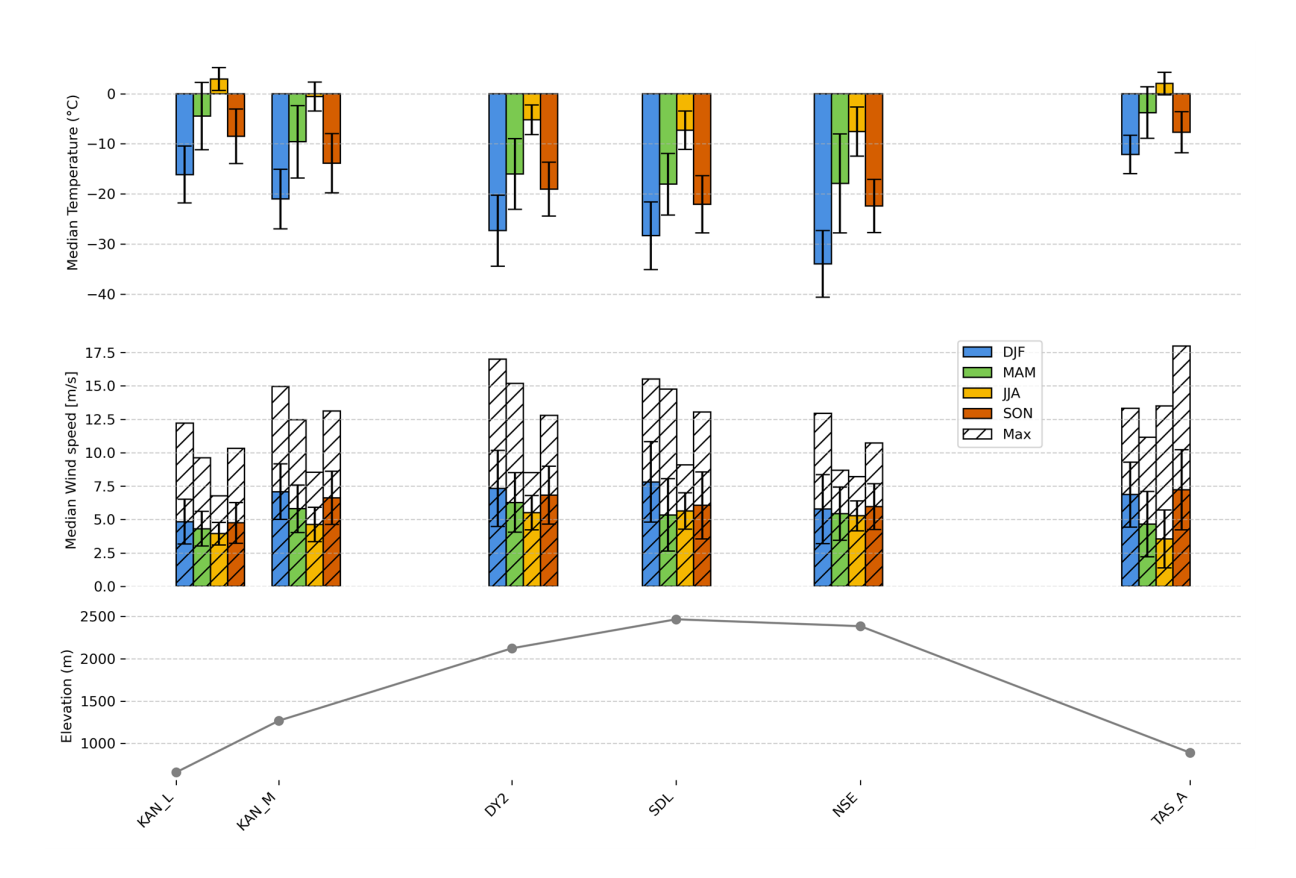


Figure 13. East-West transect starting at the KAN_L station and ending at the TAS_A station. KAN_L, KAN_M and TAS_A are ablation zone stations, while DY2, SDL and NSE are accumulation zone stations. Upper panel: Median weekly temperature for each season. Middle panel: Median weekly windspeeds. Shaded values indicate the maximum weekly wind speed for each season. Black bars indicate the standard variability of the seasonal temperatures. Lower panel: Elevation of the AWSs.





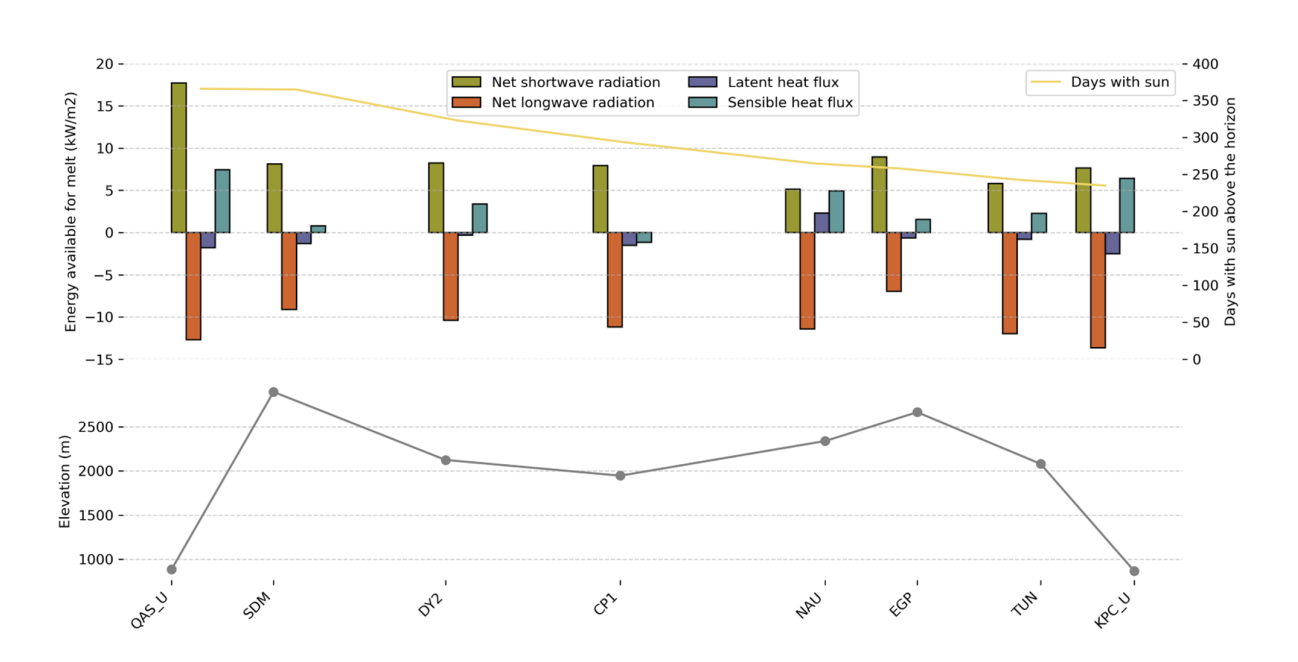


Figure 14. South-North transect of relevant variables for the surface energy balance.





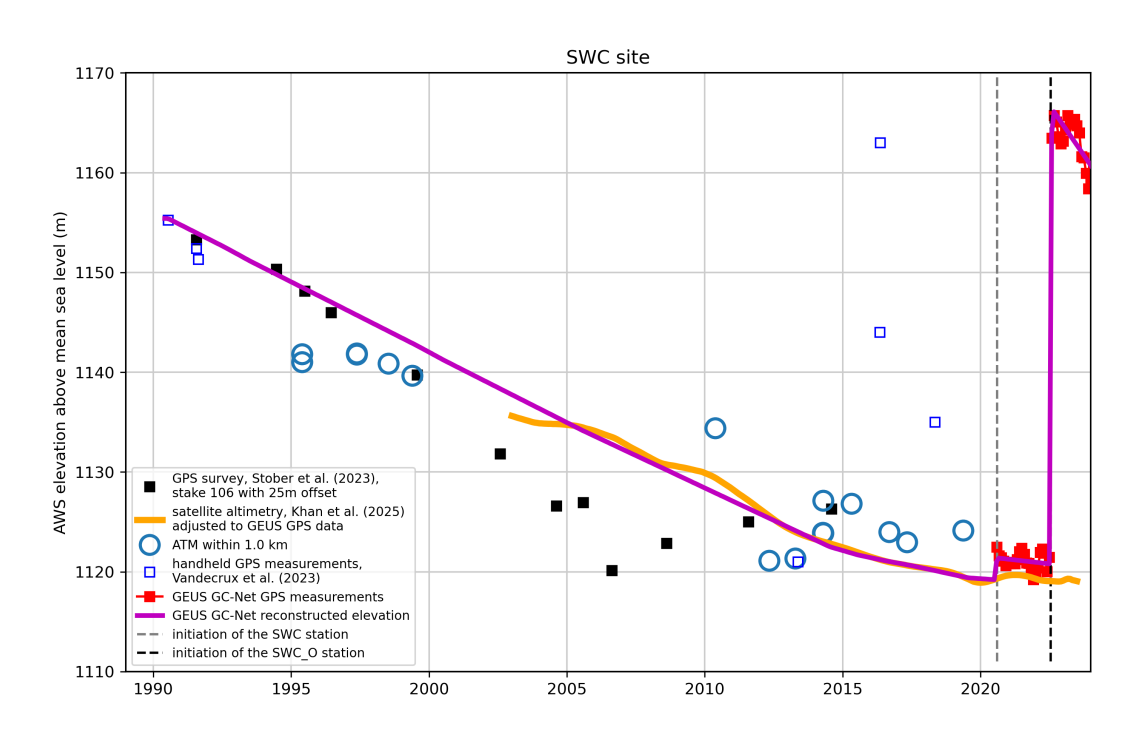


Figure 15. Example of site elevation time dependence obtained from multiple data sources.





Table 1: Information on AWS location, internal project funding, and collaboration between GEUS and externally owned AWSs.

Station ID	Latitude (°N)	Longitude (°E)	Altitude (m)	Project	AWS owned by collaborators
CEN	77.1819	-61.1160	1889	GC-NET	-
CP1	69.8708	-47.0469	1951	GC-NET	-
DY2	66.4827	-46.2954	2121	GC-NET	-
EGP	75.6282	-35.9666	2669	GC-NET	-
FRE	74.3881	-20.8334	679	GEM	GeoSphere Austria
HUM	78.5292	-56.8459	1968	GC-NET	-
JAR	69.4938	-49.6754	929	GC-NET	-
KAN_B	67.1252	-50.1832	350	PROMICE	-
KAN_L	67.1045	-49.9360	682	PROMICE	-
KAN_M	67.0686	-48.8572	1270	PROMICE	-
KAN_T	67.1510	-50.0354	498	PROMICE	-
KAN_U	67.0008	-47.0371	1844	GC-NET	-
KPC_L	79.9108	-24.0801	360	PROMICE	-
KPC_U	79.8353	-25.1605	866	PROMICE	-
LYN_L	69.3190	-53.5436	535	GEM	-
LYN_T	69.3043	-53.5902	942	GEM	-
MIT	65.6919	-37.8303	422	PROMICE	-
MIT_B	65.7061	-37.8115	519	PROMICE	Uni. Copenhagen
NAE	75.0027	-29.9778	2625	GC-NET	-
NAU	73.8405	-49.5374	2338	GC-NET	-
NEM	77.4415	-51.0845	2455	GC-NET	-
NSE	66.4774	-42.4924	2387	GC-NET	-
NUK_B	64.4615	-50.1529	107	PROMICE	Asiaq, Uni. Liverpool
NUK_K	64.1623	-51.3586	701	GEM	Asiaq
NUK_L	64.4832	-49.5243	559	PROMICE	-
NUK_N	64.9452	-49.8850	920	PROMICE	Asiaq
NUK_U	64.5084	-49.2907	1106	PROMICE	-
QAS_A	61.2430	-46.7328	1000	PROMICE	-
QAS_L	61.0306	-46.8496	224	PROMICE	-
QAS_M	61.1094	-46.8085	672	PROMICE	-

Continued on next page





Station ID	Latitude (°N)	Longitude (°E)	Altitude (m)	Project	AWS owned by collaborators
QAS_U	61.1714	-46.8234	879	PROMICE	-
RED_L	76.9256	-66.9647	768	PROMICE	Uni. Innsbruck
SCO_L	72.2155	-26.8163	435	PROMICE	-
SCO_U	72.3915	-27.2061	965	PROMICE	-
SDL	66.0002	-44.5029	2475	GC-NET	-
SDM	63.1489	-44.8174	2898	GC-NET	-
SER_B	65.6797	-37.9174	28	PROMICE	Uni. Copenhagen
SWC	69.5932	-49.2870	1152	GC-NET	-
TAS_A	65.7731	-38.8882	876	PROMICE	-
TAS_L	65.6389	-38.8992	223	PROMICE	-
TAS_U	65.6978	-38.8668	570	PROMICE	-
THU_L	76.3998	-68.2677	561	PROMICE	-
THU_L2	76.3930	-68.2654	570	PROMICE	-
THU_U	76.3901	-68.1110	745	PROMICE	-
TUN	78.0195	-33.9595	2078	GC-NET	-
UPE_L	72.8934	-54.2959	197	PROMICE	-
UPE_U	72.8847	-53.6281	906	PROMICE	-
WEG_B	71.1415	-51.2220	12	PROMICE	Uni. Graz
WEG_L	71.2046	-51.1032	930	PROMICE	Uni. Graz
ZAC_A	74.6475	-21.6520	1481	GEM	-
ZAC_L	74.6240	-21.3742	626	GEM	-
ZAC_U	74.6432	-21.4603	857	GEM	-





Table 2: Instrument information, accuracy, power, and maintenance schedule. More information on each instrument is available in Appendix.

Instrument type	Manufacturer	Model	Accuracy (Unit)	Maintenance
				schedule
Barometer	Campbell Scientific	CS100/Setra 278	±2.0 hPa	5 years
	OTT Lufft	WS401	± 1.5 hPa, ± 0.5 hPa	2 years
			(0-40°C)	
Thermometer, aspi-	Rotronic in Rotronic	MP100H-4-1-03-00-	±0.1 °C	5 years
rated	assembly	10DIN		
	OTT Lufft	WS401	± 0.2 °C (-20 to +50	2 years
			°C), ±0.5 °C (> -30	
			°C)	
	Vaisala	HMP 155E	$\pm (0.226$ - 0.0028 \times	2 years
			temperature) °C	
Hygro-	Rotronic in Rotronic	HygroClip	$\pm 0.1~\mathrm{K}, \pm 0.8\%~\mathrm{RH}$	1 year
/Thermometer,	assembly	HC2/HC2-S3		
aspirated				
Hygrometer, aspi-	OTT Lufft	WS401	$\pm 2\%$ RH	2 years
rated				
	Vaisala	HMP 155E	$\pm 0.6\%$ RH	2 years
			$(0-40\%), \pm 1.0\%$	
			RH (40–95%)	
Pluviometer	OTT Lufft	WS401	$\pm 2.0\%$	2 years
Anemometer	R.M. Young	05103-5	± 0.2 m/s or $\pm 1\%$ of	3 years
			reading	
Radiometer	Kipp & Zonen	CNR1 or CNR4	$\pm 10\%$	3 years
Sonic ranger (2)	Campbell Scientific	SR50A	± 1 cm or $\pm 0.4\%$ of	Visit
			reading	
Pressure transducer	Ørum & Jensen in	NT1400 or NT1700	$\pm 2.5~\mathrm{cm}$	5 years
	GEUS assembly			
Thermistor string	GEUS	RS PRO Thermistor,	$\pm 0.9\%$	5 years
		100 kΩ NS-25/E2		





Instrument type	Manufacturer	Model	Accuracy (Unit)	Maintenance schedule
	GEOPRECISION	Digital chip	± 0.1 °C (-5 to +50	5 years
			°C), ± 0.5 °C (-40 to	
			+85 °C)	
Inclinometer	HL Planar in GEUS assembly	NS-25/E2	±0.6%	5 years
Compass/ Inclinome-	Rion	DCM260B compass	$\pm 0.2\%$, azimuth ac-	3 years
ter		system	curacy: $\pm 0.8\%$	
GPS antenna	Trimble/Tallysman	SAF5270-	$\pm 2.5~\mathrm{m}$	5 years
		G/TW4020		
Iridium modem	NAL Research	9602-LP	-	5 years
Iridium antenna	Campbell Scientific	30741	-	5 years
Data logger	Campbell Scientific	CR1000 and	-	5 years
		CR1000X		
Battery packs	Panasonic (4 ×	LC-XC1228P, Lead	-	5 years
	28Ah)	acid		
	Panasonic (4 ×	Bk-1100FHU,	-	5 years
	60Ah)	NiMH		
	Yuasa $(6 \times 38Ah)$	NPL38-12I, Lead	-	5 years
		acid		
Solar panel	RS PRO	RS PRO 10 W	-	5 years
	RS PRO	RS PRO 20 W	-	5 years





Table 3: AWS Site Overview: Metadata for the automatic weather station networks.

Site ID	Stations composing the site	Location type	Site type	Installation date
CEN	CEN2, CEN1, GITS	Ice sheet	Accumulation	1995-06-07
CP1	CP1, CrawfordPoint1	Ice sheet	Accumulation	1995-05-23
DY2	DY2, DYE-2	Ice sheet	Accumulation	1996-05-24
EGP	EGP, EastGRIP	Ice sheet	Accumulation	2014-05-17
FRE	FRE	Local glacier	Ablation	2021-07-27
HUM	HUM, Humboldt	Ice sheet	Accumulation	1995-06-22
JAR	JAR_O, JAR, JAR1	Ice sheet	Ablation	1996-06-19
KAN_B	KAN_B	Tundra	Bedrock	2011-04-13
KAN_L	KAN_Lv3, KAN_L	Ice sheet	Ablation	2008-09-01
KAN_M	KAN_M	Ice sheet	Ablation	2008-09-02
KAN_T	KAN_Tv3	Ice sheet	Ablation	2024-05-19
KAN_U	KAN_U	Ice sheet	Accumulation	2009-04-04
KPC_L	KPC_Lv3, KPC_L	Ice sheet	Ablation	2008-07-17
KPC_U	KPC_Uv3, KPC_U	Ice sheet	Ablation	2008-07-17
LYN_L	LYN_L	Local glacier	Ablation	2021-09-01
LYN_T	LYN_T	Local glacier	Ablation	2021-09-01
MIT	MIT	Local glacier	Ablation	2009-05-04
MIT_B	MIT_B	Tundra	Bedrock	2025-08-20
NAE	NAE, NASA-E	Ice sheet	Accumulation	1997-05-03
NAU	NAU, NASA-U	Ice sheet	Accumulation	1995-05-31
NEM	NEM, NEEM	Ice sheet	Accumulation	2006-03-29
NSE	NSE, NASA-SE	Ice sheet	Accumulation	1998-04-24
NUK_B ¹	NUK_B	Tundra	Bedrock	2023-10-03
NUK_K	NUK_K	Local glacier	Ablation	2014-07-28
NUK_L	NUK_L	Ice sheet	Ablation	2007-08-20
NUK_N ¹	NUK_N	Ice sheet	Ablation	2010-07-25
NUK_U	NUK_Uv3, NUK_U	Ice sheet	Ablation	2007-08-20
QAS_A ¹	QAS_A	Ice sheet	Ablation	2012-08-20
QAS_L	QAS_Lv3, QAS_L	Ice sheet	Ablation	2007-08-24
QAS_M	QAS_Mv3, QAS_M	Ice sheet	Ablation	2016-08-11

¹ Discontinued sites.



Site ID	Stations composing the site	Location type	Site type	Installation date
QAS_U	QAS_Uv3, QAS_U	Ice sheet	Ablation	2008-08-07
RED_L	RED_Lv3	Ice sheet	Ablation	2024-08-11
SCO_L	SCO_Lv3, SCO_L	Ice sheet	Ablation	2008-07-22
SCO_U	SCO_Uv3, SCO_U	Ice sheet	Ablation	2008-07-21
SDL	SDL, Saddle	Ice sheet	Accumulation	1997-04-20
SDM	SDM, SouthDome	Ice sheet	Accumulation	1997-04-23
SER_B	SER_B	Tundra	Bedrock	2024-07-14
SWC	SWC_O, SWC, SwissCamp	Ice sheet	Ablation	1990-06-01
TAS_A	TAS_A	Ice sheet	Ablation	2013-08-28
TAS_L	TAS_L	Ice sheet	Ablation	2007-08-23
TAS_U^1	TAS_U	Ice sheet	Ablation	2008-03-11
THU_L	THU_L	Ice sheet	Ablation	2010-08-09
THU_L2	THU_L2	Ice sheet	Ablation	2022-05-16
THU_U	THU_U2v3, THU_U2, THU_U	Ice sheet	Ablation	2010-08-09
TUN	TUN, Tunu-N	Ice sheet	Accumulation	1996-05-16
UPE_L	UPE_L	Ice sheet	Ablation	2009-08-17
UPE_U	UPE_U	Ice sheet	Ablation	2009-08-18
WEG_B	WEG_B	Tundra	Bedrock	2022-06-29
WEG_L	WEG_L	Ice sheet	Ablation	2023-04-15
ZAC_A	ZAC_A	Local glacier	Accumulation	2023-04-25
ZAC_L	ZAC_Lv3	Local glacier	Ablation	2022-04-20
ZAC_U	ZAC_Uv3	Local glacier	Ablation	2022-04-21

¹ Discontinued sites.





Table 4: Data variables provided with the L3 AWS datasets

Variable Name	Units	Description
time	yyyy-mm-dd	Time stamp of hourly averages given for the following
	HH:MM:SS	hour
p_u, p_l, p_i	hPa	Air pressure (upper boom, lower boom, instantaneous)
t_u, t_l, t_i	°C	Air temperature (upper boom, lower boom, instantaneous)
rh_u, rh_l, rh_i	%	Relative humidity (upper boom, lower boom, instantaneous) with regard to water
rh_u_wrt_ice_or_water,	%	Relative humidity - adjusted for saturation over ice in
rh_l_wrt_ice_or_water,		subfreezing conditions
rh_i_wrt_ice_or_water		
qh_u, qh_l	%	Specific humidity (upper boom, lower boom)
wspd_u, wspd_l, wspd_i	m s ⁻¹	Wind speed (upper boom, lower boom, instantaneous) at
		height z_boom_u + 0.4 m
wspd_u_x, wspd_l_x, wspd_i_x	$m s^{-1}$	Directional wind speed from direction x
wspd_u_y, wspd_l_y, wspd_i_y	m s ⁻¹	Directional wind speed from direction y
wdir_u, wdir_l, wdir_i	degrees	Wind direction at height z_boom_u + 0.4 m
dsr	W m ⁻²	Downwelling shortwave radiation at height z_boom_u + 0.1 m
dsr_cor	$W m^{-2}$	Downwelling shortwave radiation – tilt-corrected
usr	W m ⁻²	Upwelling shortwave radiation at height z_boom_u + 0.1 m
dlr	$W m^{-2}$	Downwelling longwave radiation at height z_boom_u + 0.1 m
ulr	$W m^{-2}$	Upwelling longwave radiation at height z_boom_u + 0.1 m
dlhf_u, dlhf_l	W m ⁻²	Latent heat flux (upper boom, lower boom)
dshf_u, dshf_1	$\mathrm{W}~\mathrm{m}^{\text{-}2}$	Sensible heat flux (upper boom, lower boom)
albedo	-	Albedo calculated from dsr_cor and usr_cor
cc	%	Cloud cover estimated from dlr and t_u
t_surf	$^{\circ}\mathrm{C}$	Surface temperature from ulr and dlr, with emissivity =
		0.97





Variable Name	Units	Description
z_boom_u, z_boom_l	m	Boom height (upper boom, lower boom)
z_boom_cor_u, z_boom_cor_l	m	Boom height (upper boom, lower boom) - corrected for
		air temperature
z_stake	m	Height of sonic ranger on stake assembly
z_stake_cor	m	Height of sonic ranger on stake assembly - corrected for
		air temperature
z_pt, z_pt_cor	m	Depth of pressure transducer under the ice surface, cor-
		rected
z_surf_combined	m	Height of surface, combined from multiple sensors
z_ice_surface	m	Height of the ice surface for ablation stations, relative to
		installation
snow_height	m	Height of snow on glacial ice
t_i_1-11	°C	Subsurface temperature from thermistors 1–11
d_t_1-11	m	Depth of subsurface thermistors
t_i_10m	°C	10-meter subsurface temperature
precip_u, precip_l	mm	Semi-accumulated uncorrected liquid precipitation (up-
		per boom, lower boom)
rainfall_u, rainfall_l	mm	Rainfall within time step uncorrected for undercatch (up-
		per boom, lower boom)
rainfall_cor_u, rainfall_cor_l	mm	Rainfall within time step corrected for undercatch (upper
		boom, lower boom)
gps_lat	degrees north	Latitude from GNSS antenna
gps_lon	degrees east	Longitude from GNSS antenna
gps_alt	m	Altitude from GNSS antenna
lat	degrees north	Smoothed/interpolated latitude
lon	degrees east	Smoothed/interpolated longitude
alt	m	Smoothed/interpolated orthometric height
tilt_x	degrees	Tilt to east
tilt_y	degrees	Tilt to north
rot	degrees	Station rotation from true North (azimuth)
batt_v	V	Battery voltage
t_rad	°C	Radiation sensor temperature





Table 5: AWS average bias and average standard deviation between corrected and uncorrected downward solar radiation derived from the daily data product.

Station	Num_Obs	Avg_Bias	Std_Dev
CEN	5960	2.50	20.74
CP1	7523	-4.56	16.38
DY2	9686	-2.60	22.06
EGP	2672	-3.30	20.76
HUM	7899	-0.23	12.15
JAR	7616	1.79	36.28
NAE	8937	7.55	35.04
NAU	8868	-4.16	19.08
NEM	5518	3.75	22.89
NSE	8161	-15.91	42.56
SDL	9280	-2.49	27.61
SDM	9261	-22.69	47.94
SWC	9668	-4.79	14.19
TUN	9570	-1.07	8.71
KPC_U	6073	-1.19	11.86
KPC_L	5171	-3.76	31.98
SCO_L	6036	-2.89	23.07
SCO_U	5417	0.75	16.13
TAS_A	3300	-7.08	38.39
TAS_L	4828	-6.84	33.24
QAS_U	5345	-10.60	53.77
QAS_M	3096	-3.19	36.64
QAS_L	6330	-1.13	17.43
NUK_U	5308	-6.28	43.48
NUK_L	5845	-6.74	26.20
KAN_L	6070	-9.07	19.43
KAN_M	5878	-2.49	21.80
KAN_U	5388	-7.73	23.48
UPE_U	5584	-0.56	21.43
UPE_L	5694	-2.37	28.69
THU_U	4807	-5.55	21.14





Station	Num_Obs	Avg_Bias	Std_Dev
THU_L	4432	-3.23	18.43
THU_L2	1045	-2.94	18.59
MIT	4898	-5.33	24.28
WEG_B	768	58.61	67.43
WEG_L	864	0.31	27.84
FRE	1357	5.29	20.09
NUK_K	3556	-8.15	59.38
KAN_T	332	-3.73	13.99
SER_B	275	-1.15	15.93
RED_L	245	-3.33	6.90
ZAC_L	736	1.44	11.75
ZAC_U	537	3.64	10.78
ZAC_A	250	-43.93	102.07
LYN_L	1318	-25.11	58.57
LYN_T	786	-34.53	75.73





Table 6. Filtering thresholds applied to meteorological variables.

Variable	Lower Bound	Upper Bound	Season Specific
Air Temperature	5th percentile – 9°C	95th percentile + 9°C	4 separate seasons
Pressure	5th percentile – 12 hPa	95th percentile + 12 hPa	Same for all
Relative Humidity	5th percentile – 12%	95th percentile + 12%	Same for all
Wind Speed	5th percentile – 12 m/s	95th percentile + 12 m/s	Same for all





Table 7: AWS displacement statistics from monthly average GPS data.

	Latest valid date	Time span	Horizontal displacement	Elevation change
(YYYY-MM-DD)	(YYYY-MM-DD)	(yr)	(m)	(m)
2019-05-01	2025-05-01	6	20	-6
2021-06-01	2025-05-01	3.9	391	14
2022-06-01	2025-05-01	2.9	87	5
2016-06-01	2025-05-01	8.9	439	9
2021-07-01	2025-05-01	3.8	23	-3
2022-06-01	2025-05-01	2.9	49	-2
2021-05-01	2025-05-01	4	262	6
2008-09-01	2025-05-01	16.7	1742	-50
2008-09-01	2022-08-01	13.9	1449	-4
2024-05-01	2025-05-01	1	11	1
2009-04-01	2025-05-01	16.1	856	-5
2008-07-01	2025-05-01	16.8	110	-16
2008-07-01	2025-05-01	16.8	241	0
2021-09-01	2025-05-01	3.7	11	1
2021-09-01	2024-04-01	2.6	1	3
2009-05-01	2025-05-01	16	225	-34
2022-05-01	2025-05-01	3	75	-1
2021-08-01	2025-05-01	3.7	165	-4
2021-08-01	2025-05-01	3.7	25	3
2021-06-01	2025-05-01	3.9	63	2
2014-07-01	2025-05-01	10.8	7	-14
2007-08-01	2025-05-01	17.7	2323	-132
2010-07-01	2014-07-01	4	93	-9
2007-08-01	2025-05-01	17.7	2236	-41
2013-08-01	2015-08-01	2	171	-8
2007-08-01	2025-05-01	17.7	138	-96
2016-08-01	2025-05-01	8.7	248	-26
2008-08-01	2025-05-01	16.7	889	-26
2024-08-01	2025-05-01	0.7	5	-1
2008-07-01	2025-05-01	16.8	1472	-38
	2019-05-01 2021-06-01 2022-06-01 2016-06-01 2021-07-01 2022-06-01 2021-05-01 2008-09-01 2008-09-01 2008-07-01 2008-07-01 2021-09-01 2021-09-01 2021-09-01 2021-08-01 2021-08-01 2021-08-01 2021-08-01 2021-08-01 2014-07-01 2007-08-01 2013-08-01 2013-08-01 2016-08-01 2016-08-01 2024-08-01	2019-05-01 2025-05-01 2021-06-01 2025-05-01 2022-06-01 2025-05-01 2016-06-01 2025-05-01 2021-07-01 2025-05-01 2022-06-01 2025-05-01 2022-06-01 2025-05-01 2008-09-01 2025-05-01 2008-09-01 2025-05-01 2008-09-01 2025-05-01 2008-09-01 2025-05-01 2008-07-01 2025-05-01 2008-07-01 2025-05-01 2008-07-01 2025-05-01 2021-09-01 2025-05-01 2021-09-01 2025-05-01 2021-09-01 2025-05-01 2021-09-01 2025-05-01 2021-08-01 2025-05-01 2021-08-01 2025-05-01 2021-08-01 2025-05-01 2014-07-01 2025-05-01 2014-07-01 2025-05-01 2014-07-01 2025-05-01 2010-07-08-01 2025-05-01 2013-08-01 2025-05-01 2016-08-01 2025-05-01	2019-05-01 2025-05-01 3.9 2021-06-01 2025-05-01 3.9 2022-06-01 2025-05-01 2.9 2016-06-01 2025-05-01 8.9 2021-07-01 2025-05-01 3.8 2022-06-01 2025-05-01 2.9 2021-05-01 2025-05-01 4 2008-09-01 2025-05-01 16.7 2008-09-01 2025-05-01 13.9 2024-05-01 2025-05-01 1 2009-04-01 2025-05-01 16.1 2008-07-01 2025-05-01 16.8 2008-07-01 2025-05-01 3.7 2021-09-01 2025-05-01 3.7 2021-09-01 2025-05-01 3 2021-09-01 2025-05-01 3 2021-09-01 2025-05-01 3 2021-09-01 2025-05-01 3 2021-09-01 2025-05-01 3 2021-08-01 2025-05-01 3 2021-08-01 2025-05-01 3.7 2021-08-01	2019-05-01 2025-05-01 6 20 2021-06-01 2025-05-01 3.9 391 2022-06-01 2025-05-01 2.9 87 2016-06-01 2025-05-01 8.9 439 2021-07-01 2025-05-01 3.8 23 2022-06-01 2025-05-01 2.9 49 2021-05-01 2025-05-01 4 262 2008-09-01 2025-05-01 16.7 1742 2008-09-01 2025-05-01 16.7 1742 2008-09-01 2025-05-01 16.7 1742 2008-09-01 2025-05-01 1 11 2008-09-01 2025-05-01 16.1 856 2008-09-01 2025-05-01 16.8 110 2009-04-01 2025-05-01 16.8 110 2008-07-01 2025-05-01 16.8 241 2021-09-01 2025-05-01 3.7 11 2021-09-01 2025-05-01 3.7 16 2022-05-01 2025-05-0

Continued on next page





Site name	First valid date	Latest valid date	Time span	Horizontal displacement	Elevation change
	(YYYY-MM-DD)	(YYYY-MM-DD)	(yr)	(m)	(m)
SCO_U	2008-07-01	2025-05-01	16.8	1933	-19
SDL	2021-06-01	2025-05-01	3.9	13	20
SDM	2021-06-01	2025-05-01	3.9	9	6
SWC	2020-08-01	2025-05-01	4.7	559	-11
TAS_A	2013-08-01	2025-05-01	11.7	1083	-17
TAS_L	2007-08-01	2025-05-01	17.7	304	-47
TAS_U	2008-03-01	2015-08-01	7.4	400	-3
THU_L	2010-08-01	2025-05-01	14.7	62	-12
THU_L2	2022-05-01	2025-05-01	3	10	-2
THU_U	2010-08-01	2025-05-01	14.7	82	-4
TUN	2022-05-01	2025-05-01	3	80	0
UPE_L	2009-08-01	2025-05-01	15.7	23	-29
UPE_U	2009-08-01	2025-05-01	15.7	3068	-76
WEG_L	2023-04-01	2025-05-01	2.1	176	-3
ZAC_A	2023-04-01	2025-05-01	2.1	5	0
ZAC_L	2022-04-01	2025-05-01	3.1	13	-6
ZAC_U	2022-04-01	2025-05-01	3.1	61	-6





Table 8. AWS position changes for site relocations exceeding 90 m in horizontal distance

Site	Month of pre-reposition	First full month after repositioning	horizontal change (m)	Elevation change (m)
JAR	2022-07	2022-09	284	16
KAN_L	2023-07	2023-09	1278	52
NUK_L	2014-06	2014-09	94	15
NUK_L	2025-05	2025-07	1601	85
NUK_U	2013-06	2013-08	1790	12
QAS_L	2009-08	2009-09	824	46
QAS_M	2022-08	2022-09	1317	74
SWC	2022-07	2022-09	4738	44
THU_U	2018-05	2019-09	3275	-20





Appendix A: Instrument specifications

This appendix presents detailed, manufacturer-specific information for the weather station instruments used in this dataset description. The tables include specifications, model identifiers, measurement ranges, accuracies, and other relevant technical details to support data interpretation and equipment comparison.

A1 Barometers

Table A.1.1. Campbell Scientific CS100 (also known as Setra 278)

Parameter	Value	Unit
Measurement range	600 to 1100	hPa
Resolution	± 0.01	hPa
	± 0.5 @ +20	
A 2 2 2 2 2 2 2 2 2 2 2 2 2 2 2 2 2 2 2	\pm 1.0 @ 0 to +40	hPa @ °C
Accuracy	\pm 1.5 @ -20 to 0, +40 to +50	nra @ C
	\pm 2.0 @ -40 to -20, +50 to +60	
Linearity	\pm 0.4	hPa
Hysteresis	± 0.05	hPa
Repeatability	± 0.03	hPa
Long-term stability	± 0.1	$hPa yr^{-1}$
Signal output	0 to 2.5	Vdc
Warm-up time (from shutdown)	1000	millisec
Response time	< 100	millisec
Operating temperature range	-40 to +60	°C
Storage temperature range	-60 to +120	°C
Proof pressure	1500	hPa
Burst pressure	2000	hPa
Relative humidity	\leq 95, non-condensing	%





Table A.1.2. OTT Lufft WS401-UMB

Parameter	Value	Unit
Measurement range	300 to 1200	hPa
Resolution	0.1	hPa
Accuracy	\pm 0.5 @ 0 to +40	hPa @ °C
Signal output	Digital	SDI-12
Operating temperature range	-50 to +60	°C
Storage temperature range	-50 to +70	°C
Relative humidity	≤ 100	%

A2 Thermometers (aspirated)

The Rotronic RS12T contains a Pt100 temperature probe and separate hygroclip, which also incorporates a temperature probe 1195 (see A2.3). The probes are housed within an RS12T aspirated weather and radiation shield. The white shield minimises the influence of thermal radiation on temperature (and humidity) measurements, and additionally provides protection against horizontally driven rain and snow.

Table A.2.3. Rotronic Hygroclip HC2/HC2-S3 Pt100

Parameter	Value	Unit
Measurement range	-50 to +80	°C
Resolution	± 0.1	°C
Accuracy	\pm 0.1 @ +10 to +30	°C
Repeatability	0.05	°C
Long-term stability	0.1	°C yr ⁻¹





Table A.2.4. OTT Lufft WS401-UMB (thermometer parameters)

Parameter	Value	Unit
Measurement range	-50 to +60	°C
Resolution	\pm 0.1 @ -20 to +50	°C
Resolution	\pm 0.2 @ -50 to -20, +50 to +60	
Accuracy	\pm 0.2 @ -20 to +50	°C
Accuracy	\pm 0.5 @ -50 to -20, +50 to +60	
Signal output	Digital	SDI-12
Warm-up time	60	sec
Operating temperature range	-50 to +60	°C
Storage temperature range	-50 to +60	°C
Operating RH range	0 to 100	%

Table A.2.5. Vaisala HMP155E (thermometer parameters). Uses a Rika aspirated fan.

Parameter	Value	Unit
Measurement range	-80 to +60	°C
Accuracy	$\pm (0.226 - 0.0028 \times \text{temp})$ @ -80 to +20	°C
Accuracy	$\pm (0.55 - 0.0057 \times \text{temp}) @ +20 \text{ to } +60$	
Signal output	0 to 5	Vdc
Warm-up time	35	sec
Operating temperature range	-80 to +60	°C
Storage temperature range	-80 to +60	°C
Operating RH range	0 to 100	%





A3 Hygrometers (aspirated)

Table A.3.6. Rotronic Hygroclip HC2/HC2-S3

Parameter	Value	Unit
Measurement range	0 to 100	%
Accuracy	± 0.5 @ +10 to +30	% @ °C
Accuracy	\pm 0.8 @ -50 to +10, +30 to +80	
Long-term stability	<1	% yr ⁻¹
Signal output	0–1	Vdc
Warm-up time (from shutdown)	30	sec
Response time	10	sec
Operating temperature range	-50 to +80	°C
Storage temperature range	-50 to +80	°C
Operating RH range	0 to 100	%

Table A.3.7. OTT Lufft WS401-UMB

Parameter	Value	Unit
Measurement range	0 to 100	%
Accuracy	± 2	%
Signal output	Digital	SDI-12
Warm-up time (from shutdown)	60	sec
Operating temperature range	-50 to +60	°C
Storage temperature range	-50 to +60	°C
Operating RH range	0 to 100	%





A4 Pluviometer

Table A.4.8. OTT Lufft WS401-UMB (pluviometer parameters)

Parameter	Value	Unit
Measurement range	0 to 360	${ m mm~hr^{-1}}$
Resolution	0.2	mm
Accuracy	± 2	%
Signal output	Digital	SDI-12
Warm-up time (from shutdown)	60	sec
Operating temperature range	-50 to +60	°C
Storage temperature range	-50 to +60	°C
Operating RH range	0 to 100	%

1200 A5 Anemometers

Table A.5.9. Young 05103

Parameter	Value	Unit
Mangurament range	0 to 100	$\mathrm{m}~\mathrm{s}^{-1}$
Measurement range	0 to 360	0
Acqueacy	\pm 0.3 or 1 %	$\mathrm{m}~\mathrm{s}^{-1}$
Accuracy	± 3	0
Propeller diameter	0.18	m
Propeller pitch	0.294	$\mathrm{m}~\mathrm{rev}^{-1}$
Propeller distance constant	2.7	m
Propeller recovery	63	%
Damping ratio	0.3	dimensionless
Damped natural wavelength	7.4	m
Undamped natural wavelength	7.2	m
Signal output	3 pulses rev ⁻¹	V (ac)
Signal output	0 to 2.5	V (dc)
Operating temperature range	-50 to +50	°C
Storage temperature range	-50 to +50	°C
Operating RH range	0 to 100	%





Table A.5.10. Young 05108 HD-Alpine

Parameter	Value	Unit
Mangurament range	0 to 100	${ m m~s^{-1}}$
Measurement range	0 to 360	0
Acqueacy	\pm 0.3 or 1%	$\mathrm{m}~\mathrm{s}^{-1}$
Accuracy	± 3	0
Propeller diameter	0.18	m
Propeller pitch	0.50	${ m m\ rev^{-1}}$
Propeller distance constant	2.7	m
Propeller recovery	63	%
Damping ratio	0.3	dimensionless
Damped natural wavelength	7.4	m
Undamped natural wavelength	7.2	m
Signal output	3 pulses rev ^{−1}	V (ac)
Signal output	0 to 2.5	V (dc)
Operating temperature range	-50 to +60	°C
Storage temperature range	-50 to +60	°C
Operating RH range	0 to 100	%

A6 Net Radiometers

Each net radiometer is comprised of up- and down-facing pyranometers and pyrgeometers (i.e., 4 individual sensors). If the sensor type is not specified in the tables below, the value applies to all sensors.





Table A.6.11. Kipp and Zonen CNR 4

Parameter	Value	Unit
Spectral range (Pyranometer)	305 to 2800	nm
Spectral range (Pyrgeometer)	4500 to 42000	nm
Measurement range (Pyranometer)	0 to 2000	$ m W~m^{-2}$
Measurement range (Pyrgeometer)	-250 to +250	$ m W~m^{-2}$
Sensitivity (Pyranometer)	10 to 20	$\mu V (dc) (W m^{-2})^{-1}$
Sensitivity (Pyrgeometer)	5 to 15	$\mu V (dc) (W m^{-2})^{-1}$
Non-linearity	<±1	%
Field of view (Upward)	180	0
Field of view (Downward)	150	0
Long-term stability	<±1	% yr ⁻¹
Signal output (Pyranometer)	0 to 50	mV (dc)
Signal output (Pyrgeometer)	-4 to +4	mV (dc)
Response time	18	sec
Operating temperature range	-40 to +80	°C
Operating RH range	0 to 100	%





Table A.6.12. Kipp and Zonen CNR 1

Parameter	Value	Unit
Spectral range (Pyranometer)	305 to 2800	nm
Spectral range (Pyrgeometer)	4500 to 42000	nm
Measurement range (Pyranometer)	0 to 2000	$ m W~m^{-2}$
Measurement range (Pyrgeometer)	-250 to +250	$ m W~m^{-2}$
Sensitivity (Pyranometer)	10 to 35	μ V (dc) (W m ⁻²) ⁻¹
Sensitivity (Pyrgeometer)	5 to 18	$\mu V (dc) (W m^{-2})^{-1}$
Non-linearity	< ±2.5	%
Field of view (Pyranometer)	180	0
Field of view (Pyrgeometer)	150	0
Long-term stability	<±1	% yr ⁻¹
Signal output (Pyranometer)	0 to 50	mV (dc)
Signal output (Pyrgeometer)	-4 to +4	mV (dc)
Response time	18	sec
Operating temperature range	-40 to +80	°C
Operating RH range	0 to 100	%

A7 Sonic Ranger

Table A.7.13. Campbell Scientific SR50

Parameter	Value	Unit
Measurement range	0.5 to 10	m
Resolution	± 0.001	m
Accuracy	± 0.01	m
	0.4	%
Beam acceptance angle	22	0
Signal output	Digital	SDI-12
Response time	3	sec
Operating temperature range	-40 to +50	°C



1205 A8 Pressure transducer assembly

The ablation area AWSs are fitted with an Ørum & Jensen NT1400/NT1700 pressure transducer assembly (PTA), which measures changes in ice surface elevation caused by ablation. According to the manufacturer, the sensor has an accuracy of 2.5 cm. See Figure for further details on how the system is built.

A9 Thermistor Strings

1210 There are four types of thermistor strings deployed: PROMICE (8 sensors) or GC-Net (10 sensors) type, which can be either analogue or digital.

Table A.9.14. RS Pro $100k\Omega$ NTC Thermistor, 2,4 x 63,5mm

Parameter	Value	Unit
Measurement range	-80 to +150	°C
Accuracy	± 0.9	%
Response time	10	sec
Operating temperature range	-80 to +150	°C

Table A.9.15. GeoPrecision TNode Digital Thermistor

Parameter	Value	Unit
Measurement range	-40 to +85	°C
Resolution	± 0.01	°C
Aggurgay	± 0.1 @ -5 to +50	°C
Accuracy	\pm 0.5 @ -40 to -5, +50 to +85	°C
Signal output	Digital	SDI-12
Response time	1	sec
Operating temperature range	-40 to +85	°C





A10 Inclinometers

Table A.10.16. HL Planartechnik NS-25/E2 (dual axis inclinometer)

Parameter	Value	Unit
Measurement range	\pm 25	0
Resolution	0.01	0
Accuracy	0.3	0
Signal output	± 2.5	Vdc
Operating temperature range	-25 to +70	°C
Storage temperature range	-40 to +85	°C

Table A.10.17. Rion DCM260B (compass/inclinometer)

Parameter	Value	Unit
Measurement range (Heading)	0 to 360	0
Measurement range (Pitch and Roll)	\pm 85	0
Resolution	0.1	0
Accuracy (Heading)	± 0.4	0
Accuracy (Pitch and Roll)	0.1 < 15, 0.2 < 30, 0.3 < 60	0
Signal output	Digital	Serial
Response time	50	millisec
Operating temperature range	-40 to +85	°C
Storage temperature range	-40 to +100	°C

A11 GNSS Antennae

An external antenna (housed within the loggerbox) is used with the NAL 9602-LP Iridium modem, which houses an L1 GPS.

Table A.11.18. Trimble/NAL SAF5270G

Parameter	Value	Unit
Frequency	$1575.42 \pm 10 (L1)$	MHz
Gain	27	dB
Operating temperature range	-40 to +85	°C

https://doi.org/10.5194/essd-2025-687 Preprint. Discussion started: 28 November 2025 © Author(s) 2025. CC BY 4.0 License.





Table A.11.19. Calian TW4020

Parameter	Value	Unit
Frequency	$1575.42 \pm 10 (L1)$	MHz
Gain	28	dB
Operating temperature range	-40 to +85	°C





1215 Appendix B: Data product

Unrealistic spikes in the data are removed by applying predefined upper and lower thresholds to each measurement. Threshold values used in the filtering process for each measured variable are shown in the Table.

Table B.1. Threshold values used in the filtering process for each measured variable.

Variable	Units	Low threshold	High threshold
Pressure	hPa	650	1100
All temperatures	°C	-80	30
Relative humidity	%	0	100
Wind speed	${\rm m}~{\rm s}^{-1}$	0	100
Wind direction	0	0	360
Downward shortwave radiation	${ m W}~{ m m}^{-2}$	-10	1500
Upward shortwave radiation	${ m W}~{ m m}^{-2}$	-10	1000
Downward longwave radiation	${ m W}~{ m m}^{-2}$	50	500
Upward longwave radiation	${ m W}~{ m m}^{-2}$	50	500
Sensor boom height	m	0.3	3.0
Stake assembly height	m	0.3	8.0
Pressure transducer assembly	m	0	30
Precipitation	mm	0	6000
Boom tilt in both directions	0	-30	30
Latitude	°N	60	83
Longitude	$^{\circ} W$	20	70
Elevation	m	0	3000
Fan current	mA	0	200
Battery voltage	V	0	30